Observing the chain stretch transition in a highly entangled polyisoprene melt using transient extensional rheometry

Jens Kromann Nielsen and Ole Hassager
Danish Polymer Centre
Department of Chemical and Biochemical Engineering
Technical University of Denmark
DK-2800 Kgs. Lyngby, Denmark

Henrik Koblitz Rasmussen
Danish Polymer Center
Department of Mechanical Engineering
Technical University of Denmark
DK-2800 Kgs. Lyngby, Denmark

Gareth H. McKinley
Hatsopoulos Microfluids Laboratory
Department of Mechanical Engineering
Massachusetts Institute of Technology
Cambridge, Massachusetts 02139

June 8, 2009

Abstract

We measure the viscoelastic properties of a highly entangled narrow molecular weight polyisoprene melt with approximately 280 entanglements per chain in steady and transient shear and in elongational flows. The storage and loss moduli of the melt are found to be well described by the Milner and McLeish model. The relaxation modulus $G(t,\gamma)$ is measured using stress relaxation after a sudden shearing displacement and we experimentally determine the Rouse time, τ_R, by observing strain-time separability $G(t,\gamma) = G(t)h(\gamma)$ for $t > \tau_R$. The transient elongational properties are measured using three distinct instruments; the SER universal testing platform from Xpansion Instruments, its counterpart, the EVF from TA Instruments, and a Filament Stretching Rheometer. The kinematics obtained in each device are sensitive to the aspect ratio of the sample and care must be taken to achieve homogeneous deformation conditions. Especially for the SER and EVF instruments, a second aspect ratio associated with the rectangular cross-section of the sample is also important. We find that the initial growth in the tensile stress follows the prediction given by the Doi-Edwards reptation model for Deborah numbers, based on the Rouse time less than about $De_R = 0.04$. For $De_R = 0.04$ the stress difference follows more or less the Doi-Edwards prediction in the limit of infinite stretch rates and for $De_R > 0.04$ the measured stresses are well above those that can be predicted by the basic Doi-Edwards model. When $De_R > 1$ the stress difference also exceeds the linear viscoelastic prediction. In conjunction with this strain-hardening response, a stabilization is obtained whereby the limiting Hencky strain before sample rupture is markedly increased. We compare our observations in the regime $0.04 < De_R < 1$ with available experiments and theories. The stabilization for $De_R > 1$ is interpreted as a signature of chain stretching for elongational deformation rates faster than the inverse Rouse time.

1 Introduction

Non-linear rheological phenomena are encountered in polymer processing with very large deformations gradients, and arise in both shear- and extension-dominated flows. Reptational tube models identify two characteristic time constants that characterize the rheological behavior of an entangled polymer melt (Doi and Edwards, 1986). The longest time constant is the reptation time τ_d and corresponds to the time it takes for a chain to diffuse the length of its confining tube. The Rouse time τ_R is a smaller characteristic time constant and represents the time it takes a stretched chain to reach its equilibrium length in surroundings with no deformation gradients. The model of Marrucci and Grizzuti (1988) incorporates the concept of chain stretch into the tube model developed by Doi and Edwards, and predicts chain stretching in elongational flows faster than $\dot{\epsilon} \approx 1/\tau_R$, and chain orientation for flows in the intermediate region from $1/\tau_d$ to $1/\tau_R$ with no stretching. For elongational flow, we define the dimensionless Deborah number based on the Rouse time as: $De_R \equiv \dot{\epsilon}\tau_R$ and the Deborah number based on the reptation time as: $De_d \equiv \tau_d\dot{\epsilon}$. Bach et al. (2003) [5] measured transient and steady elongational viscosity for two moderately entangled polystyrene (PS) melts, with 15 and 29 entanglements respectively, and found these to display substantial strain hardening over the Doi-Edwards prediction in the intermediate regime $1/\tau_d < \dot{\epsilon} < 1/\tau_R$ and no remarkable change in behavior when entering the fastest stretching regime, $\dot{\epsilon} > 1/\tau_R$. Similarly, we have recently measured strain hardening for narrow molecular weight PS melts with 3.9 and 7.7 entanglements, (Nielsen et al. (2006)). Bach *et al.* (2003) noted that for $De_d > 1$, the stress difference at steady state scales approximately as $\sqrt{\dot{\epsilon}Z^2} \sim \sqrt{\dot{\epsilon}\tau_R}$ where Z is the number of entanglements. This holds for stress levels well above the plateau modulus. They took this scaling as an indication that chain stretch begins much sooner than the inverse Rouse time, and continues to become increasingly important with faster and faster flow.

Marrucci and Ianniruberto (2004) proposed an alternative explanation of the scaling observed

by Bach *et al.*. According to this model, the additional stress observed beyond the prediction of the Doi-Edwards model at stretch rates below the inverse Rouse time is due not to chain stretching but to the effect of a confining tube pressure. To describe this effect, they introduced a new characteristic time constant τ_p. In the Marrucci and Ianniruberto tube pressure model there are then three regions that characterize extensional flows of monodisperse polymers: 1) For $1/\tau_d < \dot{\epsilon} < 1/\tau_p$ the polymer is oriented and the tube diameter is constant; 2) for $1/\tau_p < \dot{\epsilon} < 1/\tau_R$ the polymer is oriented and the tube surrounding the chain is subject to a squeezing pressure, which reduces the tube diameter; 3) for $1/\tau_R < \dot{\epsilon}$ the polymer chains are stretched by the flow. A description of the resulting four flow regimes along with data for entangled polymer solutions and melts has recently been presented by Acharya *et al.* (2008).

The tube pressure time scales with the number of entanglements, Z, as $\tau_p \sim Z^2$, similarly to the Rouse time, meaning that the distance between τ_p and τ_d scales with Z^1, $\tau_p \sim Z^{-1}\tau_d$. Marrucci and Ianniruberto estimated τ_p to be equal to τ_d if the number of entanglements is approximately 15. The conclusions made by Bach et al. (2003) are based on two PS melts with 15 and 29 entanglement, which means that the slowest region defined as $1/\tau_d < \dot{\epsilon} < 1/\tau_p$ is not present for $Z = 15$ and is very narrow for $Z = 29$. In order to thoroughly investigate and identify the slowest region we need to be able to access a broad interval of elongational rates for which $1/\tau_d < \dot{\epsilon} < 1/\tau_p$. If for instance $\tau_p/\tau_d = 10$, the region of tube orientation should be measurable over one decade of elongational rate. This would require that $Z = 150$, which for PS corresponds to a molecular weight of $M_w = 2 \cdot 10^6\,{}^{\mathrm{g}}/_{\mathrm{mole}}$. This is however too high for rheological tests with PS melts, due to the very long relaxation times that are obtained when temperatures are restricted below the degradation temperature of around 200°C for PS. Testing of tube theories using PS will typically be limited to materials with less than 100 entanglements mainly due to its high entanglement molecular weight, $M_e = 13.3 \cdot 10^3\,{}^{\mathrm{g}}/_{\mathrm{mole}}$ and its high glass transition temperature, $T_g^{PS} = 100°\mathrm{C}$. To investigate melts with more than 100 entanglements we have thus decided to use polyisoprene

(PI) as a model material. This polymer has some of the same advantages as PS and the two materials together open a wider experimental window than may be obtained by either one alone. Both materials can be synthesized by anionic polymerization, which is the most commonly used method for making model linear polymers with low polydispersity. The side groups on PI are less bulky than is the case for PS, which results in a significant reduction of the entanglement molecular weight to $M_e = 4.82 \cdot 10^3$ g/mole (Fetters *et al.* 1994). Therefore it is possible to make materials with a larger number of entanglements giving a larger spacing between the reptation time τ_d and the tube pressure time τ_p. The less bulky side groups also lead to a significantly reduced glass transition temperature, T_g^{PI}=-75°C (compared to PS). This results in a much larger accessible frequency interval for small amplitude oscillatory shear (SAOS) measurements. Temperature sweeps in the SAOS measurements on the AR2000 rheometer show that PI is thermorheologically stable at temperatures below 100°C. PI is more prone to thermal degradation than PS due to the presence of the double bond in the backbone of the polymer; however this reduced absolute thermal stability is more than offset by the wider range of temperatures above the glass transition point that can be accessed using time-temperature superposition so that the maximum temperature for measurements become respectively $T_{max}^{PI} \cong T_g^{PI} + 175°\text{C}$ and $T_{max}^{PS} \cong T_g^{PS} + 100°\text{C}$. The rheological properties of 1,4-PI have been carefully characterized in shear over a large molecular weight range by Abdel-Goad *et al.* (2004)and Auhl *et al.* (2008). Our extensional rheological measurements build on the work of Acharya et al. (2008) for moderately entangled PI solutions and melts ($Z \leq 52$) by probing a highly entangled PI melt with $Z \sim 280$.

The SAOS test measurements have been used to estimate the reptation time, τ_d and the Rouse time of an entanglement segment, τ_e, by fitting the loss and storage moduli to the Milner and McLeish (1998) model (corrected version in Ye *et al.* 2003). The magnitude of τ_d can be roughly estimated from the position of the maximum in G'' at low frequencies, $\omega_{max} \sim 1/\tau_d$ and τ_e can be estimated from the reciprocal of the frequency at the higher of the two cross over points between

G' and G''. A number of approaches have been proposed for determining τ_R (Osaki et al. 1982). One method is to estimate the Rouse time is to use the relation $\tau_R = \tau_e Z^2$ with the value of τ_e determined from the fit to the Milner McLeish model.

A second approach is to fit the high frequency portion of the measured linear viscoelastic data to the predictions of the Rouse model:

$$G'(\omega) = G''(\omega) = a\omega^{1/2} \quad \text{for} \quad \omega \to \infty \tag{1}$$

The parameter a is given as: $a = \frac{\pi}{4}\frac{\rho RT}{M}(2\tau_R)^{1/2}$. Here ρ is the density and M is the molecular weight. Finally as a more direct way of finding the onset of chain stretch we measure the stress relaxation after a sudden shearing displacement. The Rouse time τ_R is determined experimentally by observing strain-time separability $G(t,\gamma) = G(t)h(\gamma)$ in the data for $t > \tau_R$.

We base most of our elongational conclusions on results obtained using two similar extensional rheometers, the EVF and the SER [Sentmanat et al. (2005)]. In both of these techniques a rectangular strip of polymer film is attached to two cylindrical drums that are rotated in opposite directions to each other, stretching out the sample film. To validate the strain rate in the SER-experiments we use digital video analysis of the elongational deformations at different elongational rates and for different aspect ratios of the samples. The transient elongational results obtained using the EVF and SER rheometers are also compared with elongational results on the same polymer from a filament stretching rheometer.

2 Theory

2.1 Milner- McLeish model

Milner and McLeish (1998) refined the original reptation model of Doi and Edwards (1986) by incorporating in a quantitative manner the concept of contour length fluctuation first studied by Doi and Kuzuu (1980). According to this concept, the ends of the chain do not experience the same duration of constraints as the central part of the chain, but can additionally relax stress by fluctuations along the tube length direction.

The original Milner-McLeish model (1998) has been modified by Likhtmann and McLeish (2002) who included additional details into the model, for instance constraint release. This new version of the MM model is however much more computationally demanding, and here we use the corrected version of the MM model that is described in detail in Ye et al. (2003).

2.2 Doi-Edwards model: Startup of uniaxial elongational flow

We calculate the elongational stress growth predicted by the Doi-Edwards model from the formulation described in Bird et al. (1987), which uses the independent alignment approximation. For uniaxial flow the stress becomes:

$$\sigma_{zz} - \sigma_{rr} = \int_{-\infty}^{t} M(t-t') S_{DE}(t,t') dt' \tag{2}$$

where the strain function in uniaxial elongation is:

$$\boldsymbol{S}_{DE}(t,t') = \left[\left\langle \frac{\boldsymbol{u'u'}}{u'u'} \right\rangle_{zz} - \left\langle \frac{\boldsymbol{u'u'}}{u'u'} \right\rangle_{rr} \right] = 5 \left(2e^{3\epsilon} + 1 - 3e^{3\epsilon} \frac{\arctan \sqrt{e^{3\epsilon}-1}}{\sqrt{e^{3\epsilon}-1}} \right) \frac{1}{2e^{3\epsilon}-2}. \tag{3}$$

Here $\boldsymbol{u'} = \boldsymbol{E} \cdot \boldsymbol{u}$ where $E_{ij} = \partial x / \partial x'$ is the deformation gradient from t' to t and $\langle \cdots \rangle$ indicates an average over the orientation of the 3-dimensional unit vector $\boldsymbol{u}$. The x'_i and x_i denote coordinates

of a material particle at times t' and t respectively. For startup of steady flow the Hencky strain ϵ is given as:

$$\epsilon(t,t') = \begin{cases} \dot{\epsilon}_0 t \ , & t' < 0 \\ \dot{\epsilon}_0 (t - t') \ , & 0 < t' < t \end{cases} \tag{4}$$

where $\dot{\epsilon_0}$ is the elongational rate. As an expression for the memory function $M(t)$ we use a multi mode Maxwell spectrum:

$$M(t) = \sum_{i=1}^{i_{max}} \frac{\eta_i}{\lambda_i^2} e^{-t/\lambda_i}. \tag{5}$$

A multi-mode Maxwell model can be fitted quantitatively to the rheological data obtained in SAOS and can therefore be used to calculate the linear viscoelastic prediction in transient elongation with significant accuracy. In the limit of rapid stretching, the relaxation process becomes negligible and the Doi-Edwards stress growth function in equations (3) and (4) depends only on the Hencky strain, ϵ and the plateau modulus, G_N^0 of the melt.

2.3 The Marrucci-Ianniruberto Model

Marrucci and Ianniruberto (2004) set up a balance between the force pushing on the tube from the outside with the perpendicular force from the chain inside the tube. This eventually leads to an expression for their new time constant, τ_p that is found to be:

$$\tau_p \approx \frac{a_0^2}{b^2} \tau_R \tag{6}$$

.

where a_0 is the equilibrium tube diameter, b is the length of a Kuhn step and τ_R is the Rouse time of the chain. Since a_0 and b are related to the specific type of polymer, they are independent of

molecular weight; τ_p therefore scales with molecular weight in the same way as the Rouse time, i.e: $\tau_p \sim M_w^2$. Fetters et al. (1994) report the values for the tube diameter and the Kuhn step length of 1,4 PI, (with 7% 3,4 microstructure) as $a_0 = 61.6$Å and $b = 8.44$Å, giving the pre-factor in equation 6 as $(a_0/b)^2 = 53.3$. In other words, if we define a tube pressure Deborah number defined by

$$De_p = \frac{a_0^2}{b^2} De_R \tag{7}$$

then this parameter will be given by $De_R \approx 0.02 De_p$ for the present PI. The Marrucci and Ianniruberto tube pressure model should therefore apply to the interval $0.02 < De_R < 1$.

3 Experimental Methods

3.1 Molecular characterization

The PI sample is purchased from Polymer Source Inc., Canada, which reports the mass-average molecular weight as: $M_w = 1.31 \cdot 10^6 g/mole$ and the polydispersity as $M_w/M_n = 1.1$.

The PI is characterized by H-NMR in deuterated chloroform. We determined the content of 1,4 and 3,4 structure from the chemical shift signal of the olefinic alkene protons between 4 ppm and 6 ppm, which gives a microstructural fraction of 8.6% 3,4-PI.

3.2 Shear measurements

The SAOS and step strain shear experiments are performed on an AR-G2 rheometer (TA instruments, Newcastle DE) using an 8 mm parallel plate geometry. The SAOS experiments were performed over a range of temperatures from -22°C to 75°C, and the measured values of G' and G'' were shifted horizontally to obtain the single master curve shown in Figure 1 using time-temperature shifting.

Figure 2 shows measurements of the results of the stress relaxation after a sudden shearing displacement for seven different shear strains, from $\gamma = 0.02$ to $\gamma = 0.75$ at 25°C. The limited range of shear strains presented is due to slip at the polymer-steel interface on the rheometer for strains higher than $\gamma > 0.75$. For times longer than the Rouse time, the measured moduli $G(t, \gamma)$ shown in Figure 2(a) are shifted vertically by a strain-dependent multiplier $h(\gamma)$ to determine the strain independent relaxation modulus $G(t)$. This relaxation modulus can also be evaluated from the discrete Maxwell spectrum which is independently fitted from the SAOS data. This predicted function is shown by the dashed line and accurately describes the data from 0.01 to 5000s.

3.3 Elongational viscosity measurements, SER, EVF and FSR

We present transient elongational viscosity measurements from three different instruments; the Extensional Viscosity Fixture (EVF) from TA Instruments, the Sentmanat Extensional Rheometry Rheometer fixture (SER) from Xpansion Instruments and a home built Filament Stretching Rheometer (FSR). The SER and EVF are 'constant length devices' whereas the FSR is a 'constant volume' device. On the EVF, two cylindrical drums are used to wind up a polymer sample. One cylinder rotates round its own axis while orbiting around the other cylinder which is held fixed. The fixed cylinder is mounted to the torque transducer of the ARES rheometer, and the orbiting cylinder is coupled to the ARES actuator. The Sentmanat Extensional Rheometer (SER), from Xpansion instruments, is also mounted onto the ARES rheometer and consists of two counter-rotating cylindrical drums. The polymer sample is attached onto these drums with clamps. The dimensions of the cylinders and the separation between the cylinders are the same for both the SER and the EVF, which makes it easy experimentally to compare the results from the two rheometers. We denote the radius of the cylinders by R while the distance between the attachment points for the samples is L. Then the nominal Hencky strain of the samples in the SER and EVF instruments are computed from

$$\epsilon_N = 2\theta R/L \tag{8}$$

where θ is the angle by which the cylinders have been rotated. The instantaneous nominal extension rate then becomes $\dot{\epsilon}_N = 2\Omega R/L$ where $\Omega = d\theta/dt$ is the angular velocity of the cylinders. All reported strains and strain rates for the EVF and SER instruments are nominal values, although the subscript N is omitted from $\dot{\epsilon}$.

We denote the initial thickness of the sample by W_0 and the initial height by H_0. All samples had $W_0 = 0.7$ mm, while the initial sample height was varied between $H_0 = 1.39$mm and $H_0 = 10$mm. We define the initial aspect ratio of the samples as $\Lambda_0 = H_0/W_0$. The aspect ratio H_0/L is probably also important, but it is not changed independently of Λ_0 since both L and W_0 are fixed.

In addition to the experiments on the SER and EVF we also performed experiments on the Filament Stretching Rheometer (FSR) located at DTU in Lyngby. For the FSR, the true Hencky strain and stretch rates are computed from on-line measurements of the mid-filament diameter D according to $\epsilon = 2\ln(D_0/D)$ and $\dot{\epsilon} = d\epsilon/dt$ (McKinley and Sridhar 2002, Bach *et al.* 2003a).

3.4 Strain validation by digital video microscopy

While the FSR provides immediate strain validation due to the online measurement and control of the cylindrical filament diameter via laser micrometer, the SER and EVF rheometers merely impose a torsional displacement that results in a deformation of the strip of polymer that could even be a mixture between uniaxial and planar elongation. Experience with other extensional rheometers such as the RME show that independent measurements of the kinematics is essential if the extensional viscosity is to be accurately determined (Schulze *et al.* 2001). To obtain a more direct measure of the Hencky strain imposed on the sample in the SER device we video record the

sample deformation for different elongational rates and different sample aspect ratio. We use a high-speed digital CMOS video camera (Phantom 5) operating at a frame rate of 100-1000 frames per second, depending on the stretching rate of the experiment.

4 Results and Discussion

4.1 Shear stress relaxation and Small Angle Oscillatory Shear

The measured storage- and loss moduli, G' and G'', were fitted to the MM model, and the results are shown as solid lines in Figure 1. Values of the four fitted parameters, τ_d, τ_e, Z, G_n^0 in the model are listed in table 1. In addition, a 10-mode Maxwell spectrum was also fitted to the SAOS data and is shown in Figure 1 by the dotted lines. The individual contributions to the relaxation spectrum are also listed in table 1. We report in Table 1 three distinct estimates of the Rouse time, as determined from the Milner-McLeish model, from step-strain experiments and from the high frequency limit of the Rouse model. The latter is found from equation 1 where $\rho = 830\,\mathrm{kg/m^3}$, $T = 298\,\mathrm{K}$ and $a = 860\,\mathrm{Pa\,s^{1/2}}$, see figure 1. We find good agreement between these estimates.

The strain-dependent shear modulus, determined from stress relaxation measurements can be nicely shifted onto a single master curve for elapsed times higher than a value $\tau_k = 3s$, as seen in Figure 2. The damping function determined experimentally was found to lie below the theoretical Doi-Edwards prediction $h_{DE}(\gamma)$ meaning that $h(\gamma) < h_{DE}(\gamma) < 1$ especially for $\gamma > 1$. Moreover the experimental values of $h(\gamma)$ at strains $\gamma > 0.75$ could not be reproduced when changing the gap size in the measurements. The reason for this may be that the adhesive strength of this high molecular weight PI on steel is weak, and the actual strain is smaller than the apparent strain for high values of γ. This however does not the affect the magnitude of the time τ_k which is independent of γ. Since the purpose of performing step-strain experiments in the present study is to determine this value, no investigations have been made to explore the possibility of

adhesive failure. The magnitude of the time τ_k is related to the Rouse chain stretch time, and it is expected that at short times stress relaxation occurs exponentially with the Rouse time. Doi and Edwards (1986) report the relation between τ_k and τ_R to be $4.5\tau_R = \tau_k$, and since $\exp(-\tau_k/\tau_R) = \exp(-4.5) = 0.01$ it is reasonable to assume that the chain stretch is fully relaxed after a time τ_k corresponding to 4.5 Rouse times.

We estimate the molecular weight of the PI from the number of entanglements, $Z = 280$, found by fitting the MM model to the dynamic moduli G' and G''. Auhl et al. (2008) determined an average value of the entanglement molecular weight for PI to be: $M_e = 4.82 \cdot 10^3$ g/mole, which then gives a molecular weight $M_w = 1.35 \cdot 10^6$ g/mole which serves as an additional check of the value reported by the manufacturer. The values of M_w are listed in table 1 together with the values of G_N^0 and η_0. The Rouse time found from the DE model is given as $\tau_R = \tau_e Z^2$.

Property	Value	η_i [Pa s]	λ_i [s]
η_0 from Maxwell fit to SAOS data	$3.43 \cdot 10^8$ Pa s		
τ_d from MM fit to SAOS data	646 s		
τ_R from the high frequency limit of the Rouse model	0.24 s	$2.05 \cdot 10^8$	6000
τ_R from MM fit to SAOS data	0.89 s	$1.27 \cdot 10^8$	850
$\tau_R = \tau_k/4.5$ from step strain data	0.67 s	$1.06 \cdot 10^7$	90
τ_e from MM fit to SAOS data	$1.4 \cdot 10^{-5}$ s	$6.68 \cdot 10^5$	10
s_d from MM fit to SAOS data	0.0877	45057	1
$\tau_p = a_0^2/b^2\tau_R = 53.3 \cdot 0.67s$	35.5 s	2794	0.1
G_n^0 from MM fit to SAOS data	$4.50 \cdot 10^5$ Pa	219	0.01
M_w from MM fit to Z	$1.36 \cdot 10^6$ g/mole	25.3	0.001
M_w reported by manufacturer	$1.31 \cdot 10^6$ g/mole	8.393	0.0001
Z from MM fit to SAOS data	280	5.34	$1.0 \cdot 10^{-5}$

Table 1: Properties of the polyisoprene determined from small angle oscillatory shear

4.2 Confirmation of strain rate and variation with aspect ratio

In order for the deformation in the EVF and SER to be uniaxial with constant elongational rate, the width (or thickness) and the height of the initially rectangular cross-sectional area of the

sample should decrease as $W/W_0 = \exp(-\epsilon_N/2)$ and $H/H_0 = \exp(-\epsilon_N/2)$ where ϵ_N is given by Eq. 8. We recorded the deformation of the PI film on the SER for four different imposed elongational rates: $0.2s^{-1}$, $2s^{-1}$, $8s^{-1}$ and $50s^{-1}$ using the same aspect ratio of $\Lambda_0 = 14.3$. The results are shown in Figure 3 as dimensionless height, H/H_0, against time, non-dimensionalized with the imposed elongational rate i.e. $\dot{\epsilon} \cdot t$. To examine how the actual strain obtained in the sample depends on initial aspect ratio, we also recorded the sample deformation for three different initial aspect ratios, $\Lambda_0 = 2.0$, $\Lambda_0 = 9.6$ and $\Lambda_0 = 14.3$; with all experiments carried out at the same imposed rate, $\dot{\epsilon} = 3s^{-1}$. Figure 5 displays a sequence of image frames from the videos for $\Lambda_0 = 2.0$ and 14.3, taken for frames at times t=0.0s, 0.33s, 0.66s, 1.00s and 1.33s. The height of the samples was found by digital image processing and Figure 4 shows how the dimensionless height, H/H_0, of the sample evolves with nominal strain for the three different aspect ratios.

The figure shows that the strain rate in each sample is initially constant for nominal strains lower than approximately 1.5, and then the strain rate starts to decrease. This decrease is not seen in the slowest experiment at $\dot{\epsilon} = 0.2s^{-1}$ because the sample ruptures at $\epsilon_N \approx 1.2$, nor is it seen for $\dot{\epsilon} = 50s^{-1}$ due to rupture at $\epsilon_N \approx 2.5$. By fitting the sample height, measured for $\epsilon_N < 1.2$, to the expected exponential decrease $H/H_0 = \exp(-\dot{\epsilon}t/2)$ we find that the strain rates are around 20 % smaller than the imposed strain rates. Schulze et al (2001) observed a similar deviation between the imposed strain rate and the actual strain rate for LLDPE melts on the Rheometric Scientific RME extensional rheometer. The strain rates measured from the video images are given in the caption to Figure 3.

To investigate the phenomenon further we conducted a series of experiments using samples of varying initial widths. Figure 4 shows the evolution in sample width for three different aspect ratios and the data indicates that the evolution in the actual sample deformation depends strongly on initial aspect ratio, Λ_0. As Λ_0 approaches unity the progressive deviation from ideal uniaxial elongation at high strains is greatly reduced. This phenomenon is illustrated more visually in

Figure 5.

4.3 Comparison of SER, EVF and FSR

To validate the elongational measurements made on the SER and EVF rheometers, independent measurements on the same PI were performed on an FSR rheometer, (Bach et al. 2003). The results for three different elongational rates are plotted in Figure 6 as engineering stress against the Hencky strain. For the EVF and SER we use nominal Hencky strain while for the FSR we use the Hencky strain obtained from the filament diameter. The engineering stress is defined as the measured tensile force divided by the initial cross-sectional area $(\sigma_{zz}-\sigma_{rr})_{eng} = F(t)/(H_0W_0)$. We note that the ordinate-axis is on a linear scale in order to ease visual comparison. The maximal deviation in engineering stress between the measurements on the EVF, SER and FSR at an elongational rate $\dot{\epsilon} = 0.2s^{-1}$ is 13 % at an extension of one Hencky strain unit, $\dot{\epsilon}t = 1$. Similarly the maximum deviation is 6% for $\dot{\epsilon} = 0.03s^{-1}$ at $\dot{\epsilon}t = 1$ and 7% for $\dot{\epsilon} = 0.003s^{-1}$ at $\dot{\epsilon}t = 0.5$. It can be seen that the FSR is able to measure the extensional stress growth for about 0.5 to 1.0 Hencky strain units longer than the SER and EVF. For $\dot{\epsilon} = 0.2s^{-1}$ the FSR data extend more than one Hencky strain unit further. This is due to the closed loop control of the sample deformation in the FSR. However, the SER and EVF are able to impose substantially higher elongational rates than the FSR with closed loop control in operation. The combined application of the EVF and SER fixtures with the FSR therefore allow us to explore a wider range of Deborah numbers than is possible with the FSR alone.

4.4 Transient elongational viscosity

Also shown in Figure 6 is the response of the Doi-Edwards model (Eq. 2) in the fast stretching limit $De \rightarrow \infty$. It is seen that for $De_R = 0.04$ the data follow more or less the fast stretching limit

of the Doi-Edwards model. For $De_R = 0.13$ the data lie significantly above the Doi-Edwards upper limit. Figure 7 shows the growth in the engineering stresses obtained from EVF measurements for elongational rates ranging from $\dot{\epsilon} = 0.0003s^{-1}$ to $\dot{\epsilon} = 0.6s^{-1}$ together with the corresponding Doi-Edwards prediction. The data are well predicted by the Doi-Edwards model up to a strain rate of $\dot{\epsilon} = 0.03s^{-1}$ corresponding to $De_R = 0.02$. For larger stretch rates, the data are above the Doi-Edwards model. This deviation corresponds well with the prediction of Marrucci and Ianniruberto in Eq. 7, *i.e.* we see substantial deviation from the basic Doi-Edwards theory when De_p is greater than about unity.

Figures 6 and 7 also reveal that for elongational rates below approximately $0.2s^{-1}$ the samples rupture and fail very rapidly after reaching a maximum in the engineering stress. Sample failure is seen visually as a cohesive breakage (see the pictures in Figure 7) and is also observed as a rapid decrease in the engineering stress, as opposed to the smooth decrease seen at the the highest rate of $\dot{\epsilon} = 0.6s^{-1}$. Similar observations have been reported by Wang *et al.* (2007) and Wang and Wang (2008) for a series of Styrene Butadiene Rubbers. The Considere criterion, [McKinley and Hassager (1999)], predicts that for a purely elastic material sample, failure occurs at the maximum in engineering stress:

$$\frac{\partial \sigma_{eng}}{\partial \epsilon} = 0 \tag{9}$$

.

The measured engineering stress especially for the EVF and the SER appears to satisfy this criterion for $\dot{\epsilon} < 0.2s^{-1}$. The small time delay from maximum to rupture is most likely a result of the fact that our PI is a viscoelastic rather than a purely elastic material. As mentioned, the active feedback control loop in the FSR makes it possible to delay failure to even larger Hencky strains as shown also in Figure 6.

Figure 8 shows the results of the same experiments as in Figure 7, including the results for

the highest elongational rate experiments ($0.6 \leq \dot{\epsilon} \leq 5s^{-1}$) but now plotted as the transient elongational viscosity against time together with the linear viscoelastic prediction. Figures 7 and 8 both show that the elongational behavior changes radically at an elongational rate of around $\dot{\epsilon} = 0.2s^{-1}$.

This is visually seen as stabilization of the elongating polymer filament, i.e it does not rupture for Hencky strains $\epsilon_N < 4$. The measured elongational forces also increase so the tensile stress difference exceeds not just the Doi-Edwards prediction but also the linear viscoelastic envelope. We interpret this as a sign of strain hardening for elongational rates $0.6s^{-1}$ and higher; corresponding to $De_R \geq 0.67 \times 0.6 = 0.4$.

The experiments in Figure 8, at elongational rates $\dot{\epsilon} < 0.6s^{-1}$, are performed on samples with an initial aspect ratio of $\Lambda_0 = 14.3$, whereas the experiments for $\dot{\epsilon} \geq 0.6s^{-1}$ are performed on samples with $\Lambda_0 = 2.0$. The reason for this change has already been discussed in Section 4.2. When stretching the samples to Hencky strains, $\epsilon_N > 1.2$, the local kinematics in the sample can change and the imposed deformation rate decreases for strain-hardening samples with large aspect ratios. This progressive evolution in the kinematics is reduced for aspect ratios close to unity. This improves the homogeneity of the elongational stretch history, and is why we use smaller aspect ratios in the fastest experiments. In Figure 9 we make a comparison between the measured tensile stress difference in the startup experiments performed with two different aspect ratios, $\Lambda_0 = 14.3$ and $\Lambda_0 = 2.0$. It can be seen that the stresses superpose well until total strains of $\epsilon = 3$. However beyond this point the measured stresses for $\Lambda_0 = 14.3$ begin to plateau as the effective strain rate in the sample is progressively reduced (as shown by the local slope ($d \log H/dt$) in Figures 3 and 4. By contrast, for $\Lambda_0 = 2$, the extensional stress continue to grow approximately exponentially.

The difference in elongational stresses between tests at the same strain rate with aspect ratios $\Lambda_0 = 14.3$ and $\Lambda_0 = 2.0$ is less than 35% up to a Hencky strain of $\epsilon_N = 4$. This implies that the stress measurements are not severely affected by the pronounced local change in kinematics seen

in Figure 4.

The transient elongational viscosities plotted in Figure 8 do not show any tendency to level off and approach a constant steady state elongational value in any of the experiments. At elongational rates, $\dot{\epsilon} < 0.2s^{-1}$ the cut off values in the viscosities are related to sample rupture, and the highest measured viscosity is therefore not representative of a steady state elongational viscosity. At elongational rates $\dot{\epsilon} \geq 0.6s^{-1}$ we are able to measure the transient elongational viscosity to much higher Hencky strains. However, the stress growth in Figure 9 appears to increase monotonically with strain at all strains archived experimentally.

A potential problem that one may encounter when using a rotational device such as the SER or EVF is that at Hencky strain units above $\epsilon_N = 3.8$ the polymer film has made one entire revolution on the cylindrical drum and will thus wrap completely around the clamps and come back in contact with itself. This will change the effective diameter of the drum, and thereby change the imposed elongational rate. This is a significant challenge to observing a smooth transition into a steady state viscosity for EVF and SER measurements as opposed to using a filament stretching rheometer, which in principle has no mechanical inherent restrictions on the maximum Hencky strain available. However Bach *et al.* (2003) showed that it may by necessary to adjust the rate of end-plate separation to achieve a constant elongation rate.

The fact that we have not been able to reach steady values of the stress in any nonlinear extensional experiments may be due to the very large molar mass of the PI sample. Given the number of entanglements $Z = 280$ and number of Kuhn steps $N = Za_0^2/b^2 = 15000$ we estimate that the strains needed to orient all tube segments and stretch all tube segments could be as high as $\frac{1}{2}\ln Z \approx 2.8$ and $\frac{1}{2}\ln N \approx 4.9$ respectively. However reliable viscosity data have not been obtained for nominal strains above 3.8 due to inherent limitations with the EVF and SER fixtures due to low signal to noise ratio especially for low aspect ratios as seen in Figure 4.

4.5 Stress relaxation after small strain

Nielsen *et al.* (2008) have recently reported stress relaxation measurements after elongational flow up to a total Hencky strain of $\epsilon 3$ performed in an FSR with online control of the plate motion. They found that the cessation of flow at the mid-filament was only possible by carefully adjusting the end plate separation in the relaxation phase. Without such end-plate control the nonlinear relaxation in the sample induces a slow flow that ultimately results in sample rupture as demonstrated in their Figure 2. Also Wang *et al.* (2007) employed an SER fixture on a rotational rheometer to characterize four entangled monodisperse polymer melts in extensional deformation. To investigate stress relaxation they halt the drum rotation after a given Hencky strain. They observed that when the applied initial Hencky strain is of order unity and higher the sample ultimately ruptures during the stress relaxation phase.

However, for small total strains, it is possible to measure viscoelastic stress relaxation using the SER and EVF devices by simply halting the rotation of the drums. For small strain the sample is described by the linear viscoelastic model, it may then be shown that, in the absence of fluid inertia, the fluid motion ceases as soon as the drum rotation is halted. It is an extension of the similar situation for Stokes flow of Newtonian fluids and follows in fact from the correspondence principle of linear viscoelasticty (Pipkin (1972)) as delineated in Appendix A. To demonstrate the application of the SER for stress relaxation after small strain we have included in Figure 8 experimental measurements of stress relaxation after total Hencky strains of 0.26, 0.23 and 0.345 compared with the relaxation predictions from the multimode linear Maxwell model. It is seen, that the data agree well with the predictions, which indicates that the entire fluid motion is in fact halted with no nonlinear relaxation in the sample. Keep in mind, however that in the LVE limit there is no new information in stress relaxation that we have not obtained in SAOS. The agreement between the stress relaxation experiments and the LVE predictions in Figure 8 is therefore in this situation just an internal check.

4.6 Thermal effects

When stretching the PI sample, the rate of work input to the sample would, under adiabatic conditions, result in a temperature increase as considered also by Bach *et al.* (2003). We assume initially that the sample is sufficiently thin to have a uniform temperature T throughout its width. A simple energy balance[5] then gives

$$V_0 \rho C_p \frac{dT}{dt} = (\sigma_{zz} - \sigma_{rr}) \dot{\epsilon} V_0 - h_c A_c (T - T_\infty) \tag{10}$$

where $V_0 = WHL$ is the constant sample volume and $A_c = 2HL$ is the vertical area of the sample over which heat transfer to the environment can take place. Here $W = W_0 \exp(-\epsilon/2)$ is the thickness and $H = H_0 \exp(-\epsilon/2)$ is the height of the sample, D_0 and H_0 being the initial values. Also ρ is the density, C_p the specific heat capacity of PI, h_c is the heat transfer coefficient from the vertical sides of the sample and T_∞ is the temperature of the surroundings. For simplicity we assume a constant Nusselt number $\mathrm{Nu} = h_c H / k_{air}$ where k_{air} is the thermal conductivity of the surrounding air. Equation 10 may be reformulated in the form,

$$\frac{d\Delta T}{d\epsilon} + \beta e^{\epsilon} \Delta T = \frac{1}{\rho C_p} (\sigma_{zz} - \sigma_{rr}) \tag{11}$$

where $\beta = 2\mathrm{Nu} k_{air} / (\rho C_p H_0 W_0 \dot{\epsilon})$ is a dimensionless coefficient controlling the effectiveness of heat transfer from the sample and $\Delta T = T - T_\infty$. Equation 11 can be integrated to give

$$\Delta T(\epsilon) = \frac{1}{\rho C_p} \int_0^\epsilon \exp\left(-\beta(e^\epsilon - e^{\epsilon'})\right) (\sigma_{zz}(\epsilon') - \sigma_{rr}(\epsilon'))\, d\epsilon' \tag{12}$$

We use the values $C_p = 1930 J/kgK$ and $\rho = 830 kg/m^3$ (Fetters et al. 1994 and van Krevelen 1990) for PI and $k_{air} = 0.026$W/mK for air. As an example we consider $W_0 = 0.7$mm, $H_0 = 2$mm and $\dot{\epsilon} = 5\mathrm{s}^{-1}$ corresponding to the highest stretch rates reported in the present work. To evaluate

Eq. 12 we need to determine the values of the coefficient β. With a length scale of 2 mm, radiation alone will give a Nusselt number of about 0.5. Conduction corresponds to Nu ≈ 1 while the rotation of the fixture will create a convective contribution to the heat transfer that we estimate from the Reynolds number (Re ≈ 5 for the EVF rotating fixture) and the Prandtl number Pr ≈ 0.7 by Nu $\approx 0.6\mathrm{Re}^{1/2}\,\mathrm{Pr}^{1/3} \approx 1.3$. As a conservative estimate we let the composite Nusselt number, Nu $= 2.5$ with the result that our estimate for β is about 0.01 for this experiment. To facilitate integration of Eq.12 the measured evolution in tensile stress difference vs. Hencky strain for $\dot{\epsilon} = 5\mathrm{s}^{-1}$ was fitted by a sixth order polynomial. In Table 2 we give the resulting values of the temperature increase of the PI sample obtained from eq. 12 for $\epsilon = 4$.

We estimate the corresponding changes in time constants from time-temperature superposition,

$$\tau(T + \Delta T) = \tau(T)\frac{a_{T+\Delta T}}{a_T}.$$

The Williams-Landel-Ferry shift factors are given also in Table 2(Abdel-Goad et al. (2004)).

β	0	0.01	0.1	1.0
$\Delta T[^\circ C]$	37.3	28.8	6.6	1.0
$a_{25^\circ C+\Delta T}/a_{25^\circ C}$	0.14	0.16	0.61	0.93

Table 2: Estimates of the maximum possible temperature increase for adiabatically elongated samples at high rates

It appears that one should aim for at least $\beta \geq 0.1$ for this sample and that (since we have estimated $\beta \approx 0.01$) the measurements for $\dot{\epsilon} = 5\mathrm{s}^{-1}$ should therefore be taken with considerable caution.

In closing we may check our initial assumption that the temperature of the filament is uniform throughout the strip by computing the Biot number Bi $= h_c W_0/k_{PI} = \mathrm{Nu}(k_{air}/k_{PI})(W_0/H_0)$. With the thermal conductivity of PI $k_{PI} = 0.134\mathrm{W/mK}$ we get Bi $\approx 0.17 \ll 1$ indicating that temperature variations across the filament are indeed negligible.

4.7 Rupture dynamics for EVF and SER instruments

When stretching the PI sample on the EVF or SER fixture we observe sample failure very close to the maximum of the engineering stress at elongational rates below the inverse Rouse time, $\dot{\epsilon} < \tau_R^{-1}$ whereas sample rupture occurs later for higher elongational rates. To quantify this phenomenon more clearly, in Figure 10 we show the Hencky strain at failure, $\epsilon_{failure}$ and the Hencky strain at the maximum engineering stress ϵ_{max} plotted against the Deborah number, $De_R = \dot{\epsilon} \cdot \tau_R$, based on the Rouse time ($\tau_R = 0.67s$). Also shown in the figure is the prediction for ϵ_{max} obtained from the Doi-Edwards model.

The measured values of ϵ_{max} and $\epsilon_{failure}$ are almost identical for $De_R < 0.01$ and are both predicted quite well by the Doi-Edwards model. At $De_R > 0.01$ we see that sample failure $\epsilon_{failure}$ occurs progressively later and later compared to ϵ_{max}, and the Doi-Edwards model is not able to catch the upturn in ϵ_{max} and $\epsilon_{failure}$. This progressive separation of ϵ_{max} and $\epsilon_{failure}$ is another signature of the onset of the chain-stretching as De_R exceeds a critical value. Also shown in Fig 10 by the dashed line is the empirical scaling observed by Wang et al. [24] in stretching experiments with polyisoprene, $\epsilon_{max} \sim (\tau_R \dot{\epsilon})^{1/3}$. This scaling also appears reasonably consistent with our observations for $De_R \approx O(1)$.

5 Conclusion

The aim of this work has been to investigate the transient extensional rheology of highly entangled linear polymer melts with narrow molar mass distribution. For this purpose we have utilized an ultra high molecular weight polyisoprene with a very large number of entanglements ($Z = 280$). We have measured the transient elongational stress growth using both a filament stretching device and a recently developed extensional technique in which the sample is elongated by two opposite rotating cylinders. The following conclusions can be drawn:

- The polyisoprene melt has been tested on three extensional rheometers: the SER, EVF and the FSR. For three widely separated elongational rates of $\dot{\epsilon} = 0.003, 0.06, 0.2s^{-1}$ the three rheometers obtain the same elongational properties to within 15%.

- The kinematics of the elongating melt in the EVF and SER rheometers are found to depend on the dimensions of the elongating sample. By using high speed video microscopy it is found that a high aspect ratio, (*i.e.* height-to-thickness ratio), results in a decrease in the effective elongational rate in the sample with increasing extension. This effect can be avoided or minimized by using samples with aspect ratios close to unity.

- We have not been able to attain values for a steady elongational viscosity for any of the stretch rates investigated due to rupture of the sample.

- At stretch rates up to about $De_R \simeq 0.02$, the evolution in the tensile stress difference is well described by the Doi-Edwards model.

- At stretch rates in the interval $0.02De_R < De < De_R$ the transient tensile stress difference is significantly above that predicted by the Doi-Edwards model. This regime corresponds to that investigated by Bach *et al.* (2003) for a linear PS melt.

- At stretch rates smaller than the inverse Rouse time, $De_R < 1$, sample failure is observed in general accordance with the Considère criterion, that is, at the maxima in the engineering stress, or at most one Hencky strain unit later.

- At stretch rates higher than the inverse Rouse time, $De_R > 1$, the sample is stable to strains substantially beyond the Considere criterion and significant strain hardening in the transient stress growth can be measured.

While we feel justified to interpret the stabilization for stretch rates $De_R > 1$ to molecular stretching we do not offer a unique explanation for the increase of the stresses above the Doi-Edwards

model in the interval $0.02De_R < De < De_R$. Two interpretations that have been proposed are that some molecular stretching does take place also in this regime (Bach *at al.* (2003)) or that the increased stresses are due to the tube pressure effect (Marrucci and Iannirubertо (2004)). The latter interpretation does predict the lower limit for this region in reasonable agreement with our data. However it may not be possible to distinguish between these two interpretations from rheological measurements alone and it would be useful in the future to augment this data with birefringence measurements.

6 Appendix: Application of the correspondence principle to stress relaxation

The fact that no flow will take place after the drum rotation is halted relies on two conditions. First that inertia, gravity and surface tension are negligible, and second that the deformation is small so the material is described by the theory of linear viscoelasticity. To illustrate the generality of the situation, consider a viscoelastic material where the boundary is divided into two parts, Γ_u on which the velocity $\boldsymbol{v}$ is given and Γ_f on which the surface force per unit area is specified. Assume furthermore, that the boundary conditions on Γ_v may be factorized into a spatial and temporal component so that

$$\boldsymbol{v}(\Gamma_v) = \boldsymbol{g}(\boldsymbol{x})f(t)$$

for some given functions $\boldsymbol{g}$ and f. On Γ_f we assume equilibrium with the surroundings so that

$$\boldsymbol{n} \cdot \boldsymbol{\sigma}(\Gamma_f) + \boldsymbol{n}p(\Gamma_f) = \boldsymbol{n}p_{atm}$$

where $\boldsymbol{n}$ is an outward unit normal to Γ and p_{atm} is the air pressure.
In the absence of inertia, the linear momentum equation in the fluid domain reads

$$\boldsymbol{\nabla} \cdot \boldsymbol{\sigma} - \boldsymbol{\nabla}p = 0$$

while the LVE constitutive equation is

$$\boldsymbol{\sigma}(\boldsymbol{x}, t) = \int_{-\infty}^{t} G(t - t')\dot{\boldsymbol{\gamma}}(\boldsymbol{x}, t')dt' \tag{13}$$

We now try a solution of the form $\boldsymbol{v}(\boldsymbol{x},t) = \boldsymbol{v}_0(\boldsymbol{x})f(t)$ where f is the function specified by the boundary conditions. The corresponding stresses become

$$\boldsymbol{\sigma}(\boldsymbol{x},t) = \int_{-\infty}^{t} G(t-t')f(t')dt' \, \dot{\boldsymbol{\gamma}}_{\mathbf{0}}(\boldsymbol{x}) = \mu(t) \, \dot{\boldsymbol{\gamma}}_{\mathbf{0}}(\boldsymbol{x})$$

where $\dot{\boldsymbol{\gamma}}_{\mathbf{0}}(\boldsymbol{x}) = \boldsymbol{\nabla}\boldsymbol{v}_0 + (\boldsymbol{\nabla}\boldsymbol{v}_0)^{\dagger}$ is the rate-of-deformation tensor corresponding to $\boldsymbol{v}_0$ and the function $\mu(t)$ is defined for convenience. Let $p = p_0(\boldsymbol{x}) \, \mu(t) + p_{atm}$. Then it follows that we need to find solutions to the Stokes problem:

$$\boldsymbol{\nabla} \cdot \boldsymbol{v}_0 = 0$$

$$\nabla^2 \boldsymbol{v}_0 - \boldsymbol{\nabla} p_0 = 0$$

$$\boldsymbol{v}_0(\Gamma_v) = \boldsymbol{g}(\boldsymbol{x})$$

$$\boldsymbol{n} \cdot \dot{\boldsymbol{\gamma}}_{\mathbf{0}}(\boldsymbol{x})(\Gamma_f) + \boldsymbol{n} p_0 = 0$$

There is no time dependence in this problem, and solutions for $\boldsymbol{v}_0$ and p_0 can, in principle, be found. Therefore the trial solution $\boldsymbol{v}(\boldsymbol{x},t) = \boldsymbol{v}_0(\boldsymbol{x})f(t)$ is indeed a solution to the LVE flow problem. This implies, that in the absence of inertia, the flow is stopped in the entire domain as soon as $f(t) = 0$ corresponding in our situation to the stopping of the drum rotation. Thus there is no sample flow or deformation in the stress relaxation phase for small deformations. The boundary conditions have been applied at fixed $\boldsymbol{x}$ values. That is, we have not taken into account the deformation of the fluid domain that results from the drum rotation. This is in agreement with the assumptions in the application of small strain linear viscoelasticity. The conclusion reached above can also be made on the basis of the correspondence principle of linear viscoelasticty as described by Pipkin (1972).The argument gives a theoretical basis for the application of the EVF,

SER and FSR (without end-plate control) to the measurement of tensile stress relaxation in the small strain limit.

References

[1] Abdel-Goad, M., W. Pyckhout-Hintzen, S. Kahle, and Allgaier, J., Richter, D. and Fetters, L.J. , "Rheological properties of 1,4-polyisoprene over a large molecular weight range," Macromolecules **37**, 8135-8144 (2004).

[2] Acharya, M.V., P.K. Bhattacharjee, D.A. Nguyen and T. Sridhar, "Are entangled polymer solutions different from melts?" The XVth International Congress on Rheology, The Society of Rheology 80th Annual Meeting edited by A. Co, L. G. Leal, R. H. Colby and A. J. Giacomin; American Institute of Physics (2008)

[3] Auhl, D., J. Ramirez, A. E. Likhtman, T. C. B. McLeish, P. Chambon, and C. M. Fernyhough, "Linear and nonlinear shear flow behavior of monodisperse polyisoprene melts with a large range of molecular weights," J. Rheol. **52**, 801-835 (2008)

[4] Bach, A., H.K. Rasmussen and O. Hassager, "Extensional viscosity for polymer melts measured in the filament stretching rheometer," J. Rheol. J. **47**, 429-441 (2003)

[5] Bach A., K. Almdal, H.K. Rasmussen and O. Hassager, "Elongational viscosity of narrow molar mass distribution polystyrene," Macromolecules **36**, 5174-5179 (2003a).

[6] Bird, R. B., Curtiss, C. F., Armstrong, R. C. and Hassager, O., *Dynamics of Polymeric Liquids*, II, *Kinetic Theory* (Wiley, New York 1987).

[7] Doi, M., S. F. Edwards, *The Theory of Polymer Dynamics* (Clarendon Press, Oxford, 1986).

[8] Doi, M., Kuzuu, N. Y. , "Rheology of star polymers in concentrated solutions and melts," J. Polymer Science **18**, 775-780 (1980).

[9] Fetters, L. J.; Lohse, D. J.; Richter, D.; Witten, T. A.; Zirkel, A. "Connection between polymer molecular weight, density, chain dimensions, and melt viscoelastic properties" Macromolecules, **27**, 4639-4647, (1994)

[10] Likhtman, A. and T. C. B. McLeish, "Quantitative theory for linear dynamics of linear entangled polymers," Macromolecules **35**, 6332-6343 (2002)

[11] Marrucci, G., G. Ianniruberto, "Interchain pressure effect in extensional flows of entangled polymer melts," Macromolecules, **37**, 3934-3942 (2004).

[12] Marrucci, G., N. Grizzuti, "Fast flows of concentrated polymers - Predictions of the tube model on chain stretching ," Gazz. Chim. Ital. **118**, 179-185 (1988).

[13] McKinley G. H., O. Hassager, "The Considére condition and rapid stretching of linear and branched polymer melts", J. Rheol. **43**, 1195-1212 (1999).

[14] McKinley, G.H., T. Sridhar, "Filament-stretching rheometry of complex fluids" Annu. Rev. Fluid Mech. **34** 375-415 (2002).

[15] Milner, S. T., T. C. B. McLeish, "Reptation and contour-length fluctuations in melts of linear polymers,". Phys. Rev. Lett. **81**, 725-728 (1998).

[16] Nielsen, J. K., H. K. Rasmussen, O. Hassager and G. H. McKinley, "Elongational viscosity of monodisperse and bidisperse polystyrene melts, " J. Rheol. **50**, 453-476 (2006).

[17] Nielsen, J.K., H.K. Rasmussen and O. Hassager, "Stress relaxation of narrow molar mass distribution polystyrene following uniaxial extension," J. Rheol. **52**, 885-899 (2008)

[18] Osaki K., K. Nishizawa and M. Kurata, "Material Time Constant Characterizing the Nonlinear Viscoelasticity of Entangled Polymeric Systems," Macromolecules **15**, 1068-1071 (1982).

[19] Pipkin, A. C., *Lectures in viscoelasticity theory* (Springer Verlag, 1972)

[20] Schulze, J. S., T. P. Lodge, C. W. Macosko , J. Hepperle, H. Münstedt, H. Bastian, D. Ferri, D. J. Groves, Y. H. Kim, M. Lyon, T. Schweizer, T. Virkler, E. Wassner,W. Zoetelief, "A comparison of extensional viscosity measurements from various RME rheometers," Rheol. Acta **40**, 457-466 (2001).

[21] Sentmanat, M., B. N. Wang, G. H. McKinley, "Measuring the transient extensional rheology of polyethylene melts using the SER universal testing platform," J. Rheol. **49**, 585-606 (2005).

[22] Van Krevelen, D.W., *Prediction of Polymer Properties* (Elsevier, Oxford, 1990.)

[23] Wang, Y., Boukany, P., Wang, S.Q. and Wang, X., "Elastic breakup in uniaxial extension of entangled polymer melts", Phys. Rev. Lett. **99**, 237801 (2007).

[24] Wang, Y., Wang, S., "From elastic deformation to terminal flow of a mono disperse entangled melt in uniaxial extension" J. Rheol. **56**, 1275-1290 (2008).

[25] Ye, X., Larson, R.G., Pattamaprom, C. and Sridhar, T., "Extensional properties of monodisperse and bidisperse polystyrene solutions, " J. Rheol. **47**, 443-468 (2003).

7 Figure captions

Figure 1: Measurements of G' and G'' obtained from small amplitude oscillatory shear experiment. AR-G2 (TA Instruments) 25°C. The solid lines (——) are the Milner McLeish prediction for $Z = 280$, $\tau_e = 2.0 \cdot 10^{-5}s$, and $G_N^0 = 450$kPa. The dotted lines (- - - -) are calculated from the Maxwell spectrum, table 1, with $i_{max} = 10$. The dash dotted line line is $G' = 860\omega^{1/2}$.

Figure 2: Measurements of (a) $G(t,\gamma)$ (b) $G(t,\gamma)/h(\gamma)$, for discrete values of the applied strain $\gamma \in [0.01; 0.75]$ increasing from top to bottom. The dotted line is the predicted variation in $G(t)$ from the Maxwell coefficients fitted to the small amplitude oscillatory shear measurements. AR-G2 (TA Instruments) 25°C.

Figure 3: Development of the normalized height of the polyisoprene film in the SER extensional rheometer as function of nominal Hencky strain for four nominal elongational rates and initial aspect ratio $\Lambda_0 = 14.3$ (25°C). Dotted lines are the predicted behaviour from the nominal elongational rates assuming uniaxial extension. The elongational rates found from the initial linear slope (on this semilogarithmic scale for , $\dot{\epsilon} \cdot t < 1.2$) are respectively $\dot{\epsilon} = 0.177s^{-1}$, $\dot{\epsilon} = 1.812s^{-1}$, $\dot{\epsilon} = 6.77s^{-1}$ and $\dot{\epsilon} = 41.9s^{-1}$.

Figure 4: Normalized height of the polyisoprene film in the SER extensional rheometer as function of the nominal Hencky strain for different aspect ratios, $\Lambda_0 = 2.0$, $\Lambda_0 = 9.6$ and $\Lambda_0 = 14.3$ at the same nominal elongational rate of $\dot{\epsilon} = 3s^{-1}$ (25°C). The data is taken from images obtained by high speed video microscopy. The ideal uniaxial kinematic response is shown by the dotted line. Ideal planar extension would correspond to a horizontal line. For $\Lambda_0 \gg 2.0$ the deformation is seen to be a mixture of uniaxial and planar extension.

Figure 5: Black and white image frames from the video for $\Lambda_0 = 2.0$ and $\Lambda_0 = 14.3$ from the SER instrument. The nominal elongational rate is $\dot{\epsilon} = 3s^{-1}$ in both experiments. Close inspection of the frames show that the kinematics depend on the aspect ratio, as shown in Figure 4.

Figure 6: Measurements of the engineering stress for $\dot{\epsilon} = 0.003s^{-1}$, $\dot{\epsilon} = 0.06s^{-1}$ and $\dot{\epsilon} = 0.2s^{-1}$ as function of Hencky strain as determined by the EVF, SER and FSR instruments (25°C). For the EVF and SER, ϵ is nominal Hencky strain (Eq. 8) while for the FSR ϵ is computed from the instantaneous filament diameter. The Rouse Deborah numbers for the three experiments are $De_R = 0.002$, $De_R = 0.04$ and $De_R = 0.13$, based on the Rouse time of $\tau_R = 0.67s$. The solid line is the Doi-Edwards prediction, equation 3, for $De_d \gg 1$, with $G_n^0 = 450kPa$

Figure 7: Transient growth of the engineering stress for elongational rates : $\dot{\epsilon} = 0.0003s^{-1}$ +, $\dot{\epsilon} = 0.0006s^{-1}$ $\triangledown$, $\dot{\epsilon} = 0.001s^{-1}$ $\blacktriangle$, $\dot{\epsilon} = 0.003s^{-1}$ $\triangle$, $\dot{\epsilon} = 0.006s^{-1}$ $\Diamond$, $\dot{\epsilon} = 0.01s^{-1}$ $\circ$, $\dot{\epsilon} = 0.03s^{-1}$ $\blacktriangledown$, $\dot{\epsilon} = 0.06s^{-1}$ $\square$, $\dot{\epsilon} = 0.1s^{-1}$ $*$, $\dot{\epsilon} = 0.2s^{-1}$ $\blacksquare$, and $\dot{\epsilon} = 0.6s^{-1}$ $\bullet$. (EVF instrument, 25°C). The dotted lines are the prediction of the Doi-Edwards model for the seven lowest elongational rates, and the solid line is the rapid stretching limit of the Doi-Edwards model, (equation 3) . The bottom frames show the development of the polyisoprene sample at different times stretched at a rate of $\dot{\epsilon} = 0.2s^{-1}$.

Figure 8: Transient elongational viscosity for 12 elongational rates from $\dot{\epsilon} = 0.0006s^{-1}$ to $\dot{\epsilon} = 5.0s^{-1}$. The solid line is the linear viscoelastic envelope (EVF instrument, 25°C). Also included is the transient elongational viscosity measured during startup and stress relaxation for $\dot{\epsilon} = 0.1s^{-1}$ stretched to $\blacksquare$ $\epsilon = 0.26$, $\bullet$ $\dot{\epsilon} = 0.01s^{-1}$ stretched to $\epsilon = 0.23$ and $\blacktriangle$ $\dot{\epsilon} = 0.003s^{-1}$ stretched to a final strain $\epsilon = 0.345$. The dotted lines are the relaxation prediction during relaxation from the

multimode linear Maxwell model.

Figure 9: Comparison between the transient extensional stress for elongational experiments performed with initial aspect ratio of $\Lambda_0 = 2.0$ and $\Lambda_0 = 14.3$ respectively (EVF instrument, 25°C). The imposed elongational rates range from $\dot{\epsilon} = 0.6s^{-1}$ to $\dot{\epsilon} = 5s^{-1}$. The solid line is the Neo-Hookean prediction, $\sigma_{zz} - \sigma_{rr} = G_N^0(e^{2\epsilon} - e^{-\epsilon})$ and the dotted line is the rapid stretching limit from the Doi-Edwards equation from eq. 3.

Figure 10: Measured values of Hencky strain at which the engineering stress goes through a maximum (ϵ_{max}) and Hencky strain at which the sample ruptures ($\epsilon_{failure}$). Also shown is the Doi-Edwards prediction of ϵ_{max}.

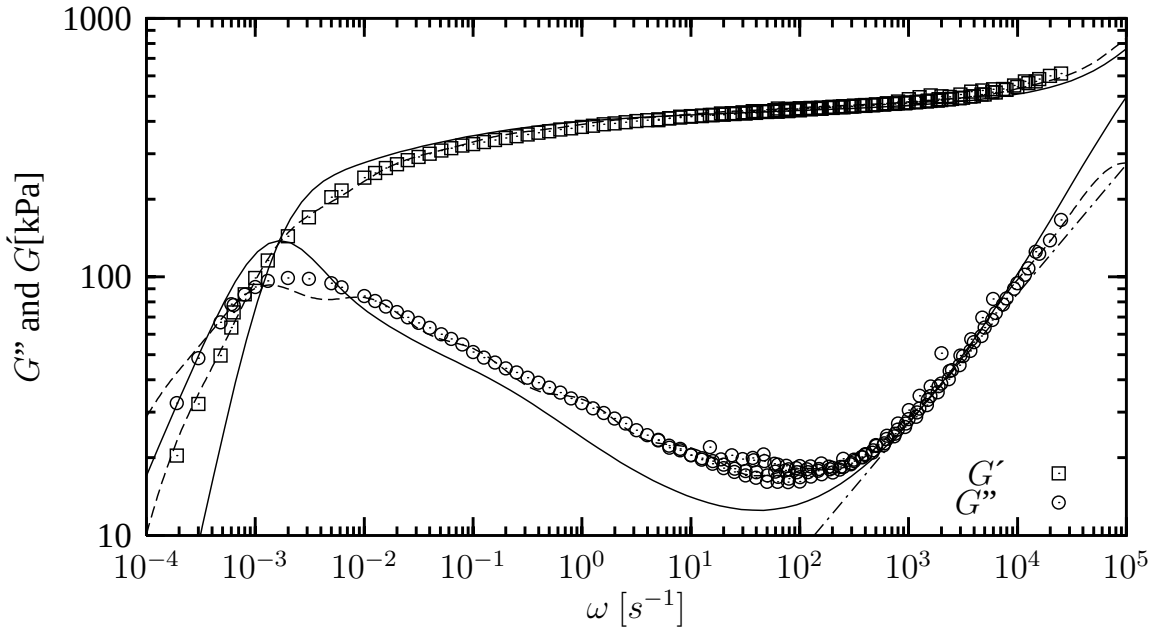
1000
100
10
G” and G´[kPa]
10^{-4}
10^{-3}
10^{-2}
10^{-1}
10^{0}
10^{1}
10^{2}
10^{3}
10^{4}
10^{5}
ω $[s^{-1}]$
G´
G”

Figure 1:

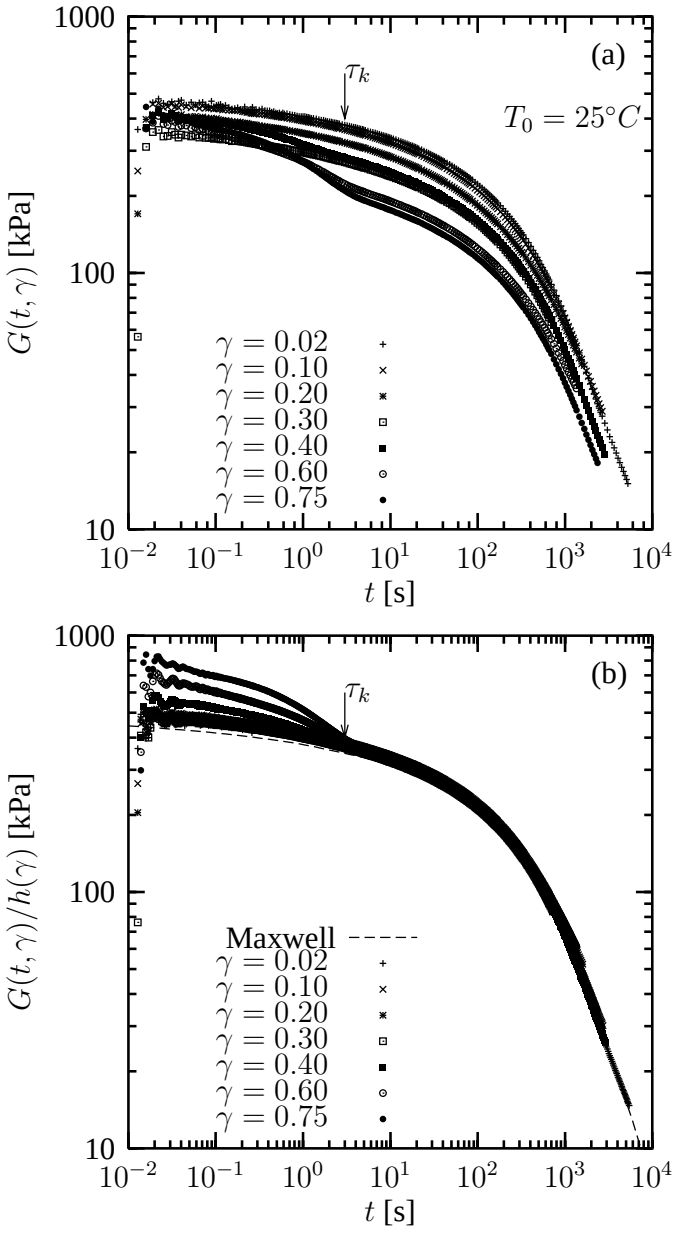
1000
100
10
(a)
τ_k
$T_0 = 25°C$
$G(t,\gamma)$ [kPa]
$\gamma = 0.02$
$\gamma = 0.10$
$\gamma = 0.20$
$\gamma = 0.30$
$\gamma = 0.40$
$\gamma = 0.60$
$\gamma = 0.75$
10^{-2} 10^{-1} 10^{0} 10^{1} 10^{2} 10^{3} 10^{4}
t [s]
1000
100
10
(b)
τ_k
$G(t,\gamma)/h(\gamma)$ [kPa]
Maxwell
$\gamma = 0.02$
$\gamma = 0.10$
$\gamma = 0.20$
$\gamma = 0.30$
$\gamma = 0.40$
$\gamma = 0.60$
$\gamma = 0.75$
10^{-2} 10^{-1} 10^{0} 10^{1} 10^{2} 10^{3} 10^{4}
t [s]

Figure 2:

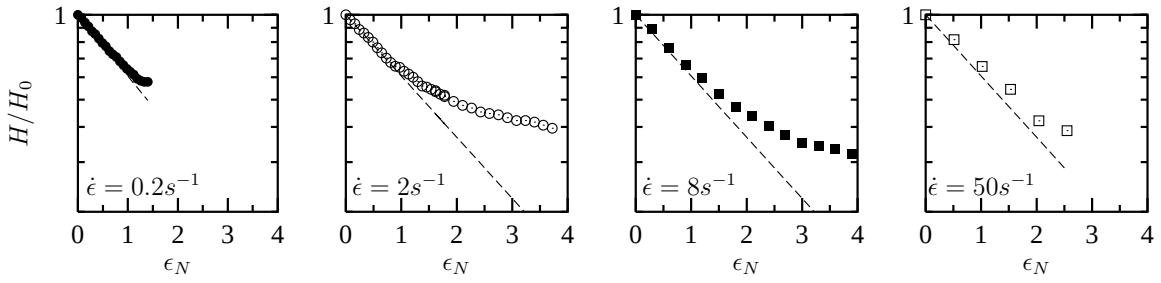
1
H/H_0
$\dot{\epsilon} = 0.2s^{-1}$
$\dot{\epsilon} = 2s^{-1}$
$\dot{\epsilon} = 8s^{-1}$
$\dot{\epsilon} = 50s^{-1}$
0 1 2 3 4
ϵ_N

Figure 3:

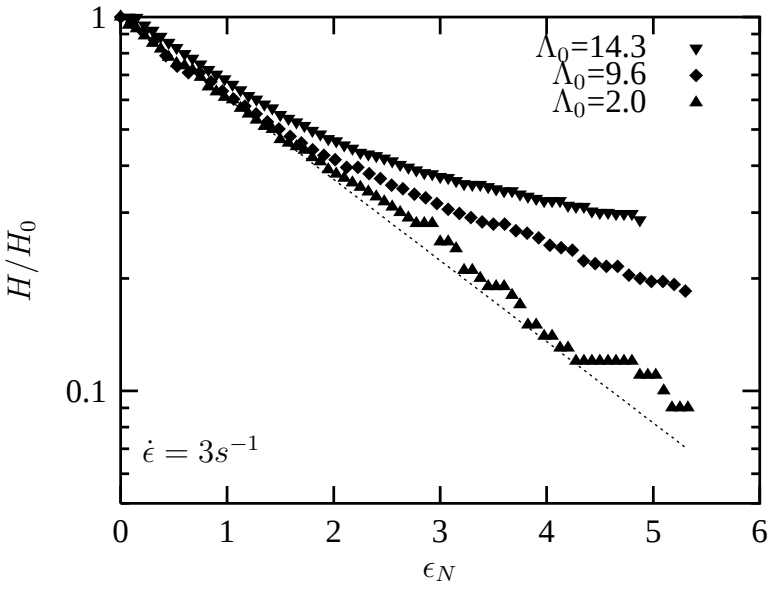
1
0.1
H/H_0
Λ_0=14.3
Λ_0=9.6
Λ_0=2.0
$\dot{\epsilon} = 3s^{-1}$
0
1
2
3
4
5
6
ϵ_N

Figure 4:

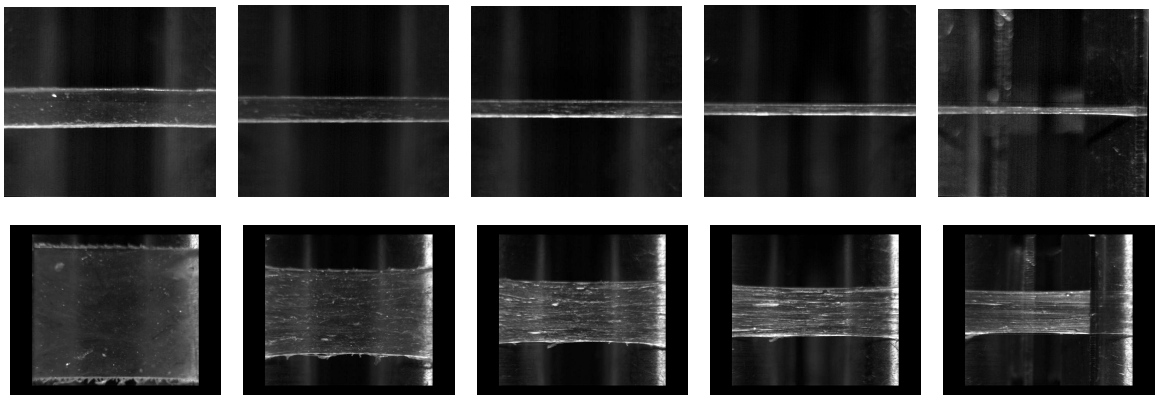

$\epsilon_N = 0$ $\epsilon_N = 1$ $\epsilon_N = 2$ $\epsilon_N = 3$ $\epsilon_N = 4$

Figure 5:

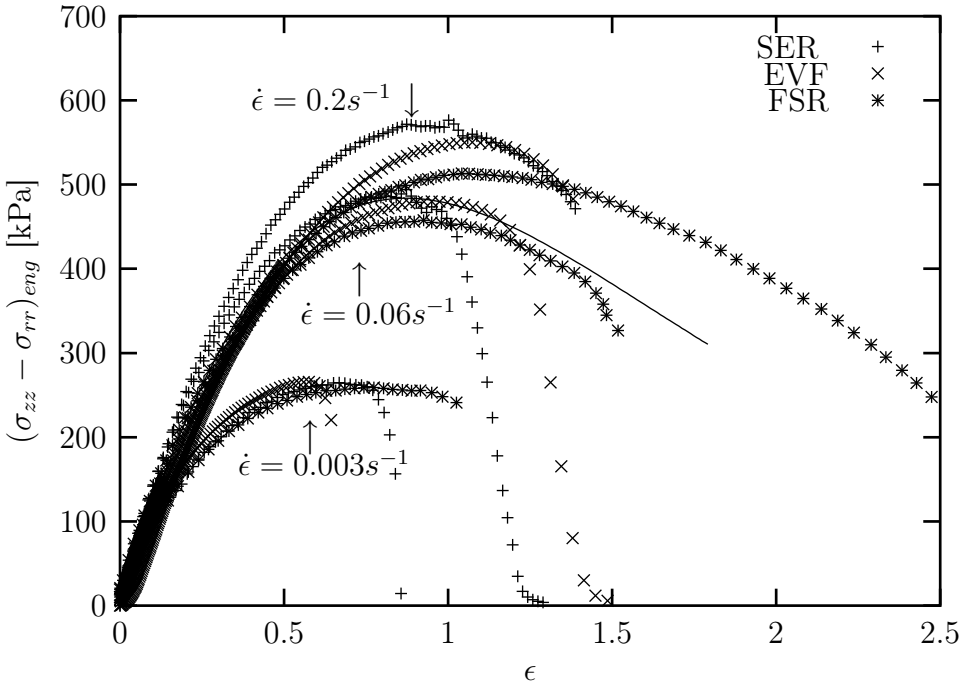
SER
EVF
FSR
$\dot{\epsilon} = 0.2s^{-1}$
$\dot{\epsilon} = 0.06s^{-1}$
$\dot{\epsilon} = 0.003s^{-1}$
$(\sigma_{zz} - \sigma_{rr})_{eng}$ [kPa]
ϵ
0
100
200
300
400
500
600
700
0
0.5
1
1.5
2
2.5

Figure 6:

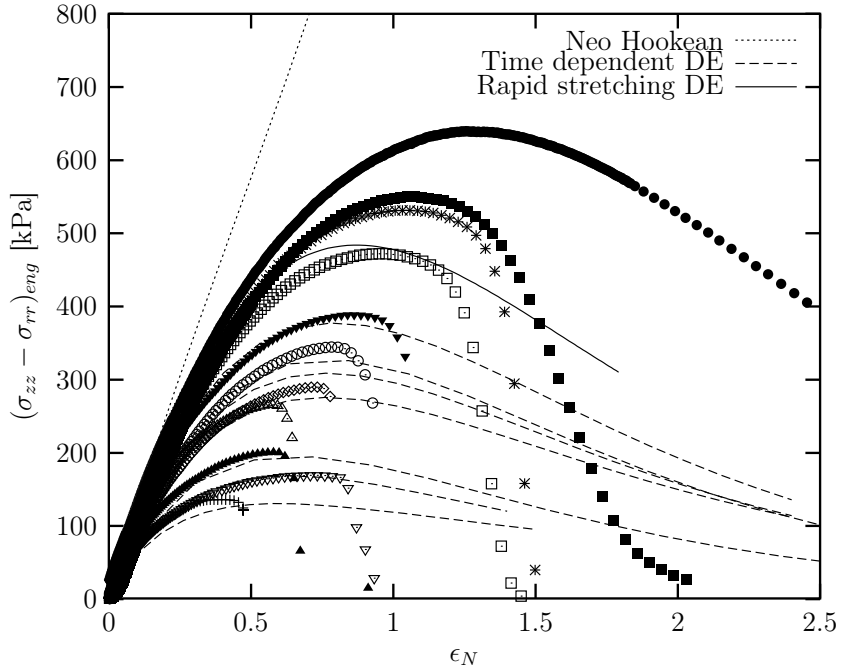

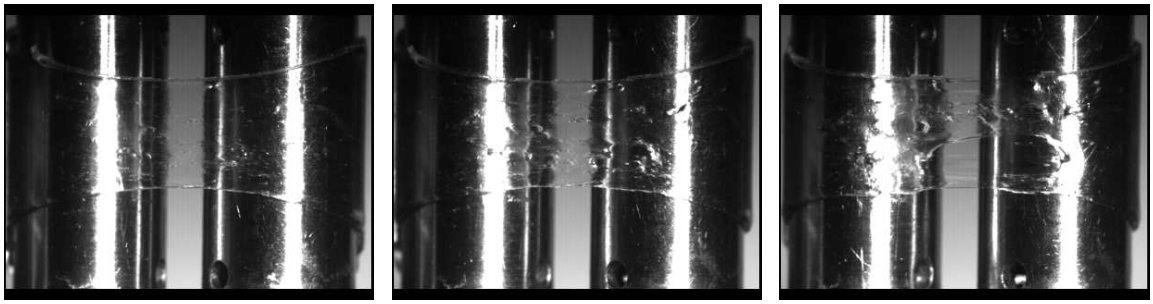

$\epsilon_N = 1.300$ $\epsilon_N = 1.433$ $\epsilon_N t = 1.567$

Figure 7:

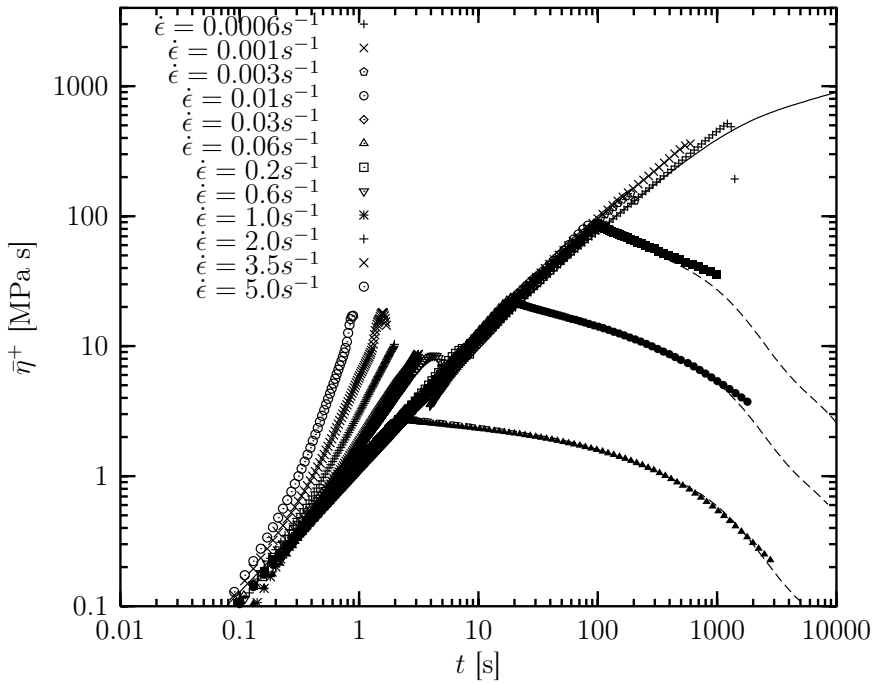
$\dot{\epsilon} = 0.0006s^{-1}$
$\dot{\epsilon} = 0.001s^{-1}$
$\dot{\epsilon} = 0.003s^{-1}$
$\dot{\epsilon} = 0.01s^{-1}$
$\dot{\epsilon} = 0.03s^{-1}$
$\dot{\epsilon} = 0.06s^{-1}$
$\dot{\epsilon} = 0.2s^{-1}$
$\dot{\epsilon} = 0.6s^{-1}$
$\dot{\epsilon} = 1.0s^{-1}$
$\dot{\epsilon} = 2.0s^{-1}$
$\dot{\epsilon} = 3.5s^{-1}$
$\dot{\epsilon} = 5.0s^{-1}$
$\bar{\eta}^+$ [MPa s]
t [s]
0.1
1
10
100
1000
0.01
0.1
1
10
100
1000
10000

Figure 8:

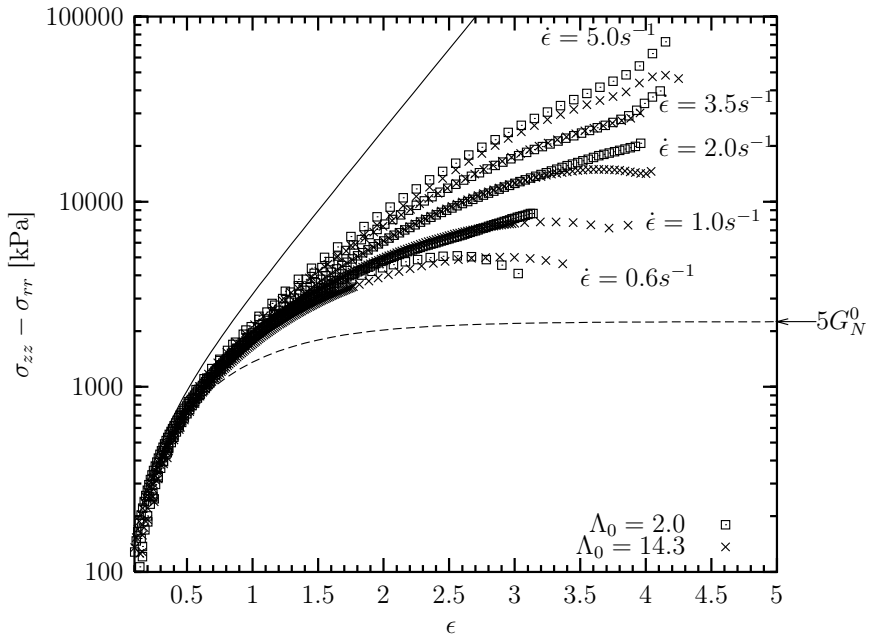
100000
10000
1000
100
0.5
1
1.5
2
2.5
3
3.5
4
4.5
5
ϵ
$\sigma_{zz} - \sigma_{rr}$ [kPa]
$\dot{\epsilon} = 5.0s^{-1}$
$\dot{\epsilon} = 3.5s^{-1}$
$\dot{\epsilon} = 2.0s^{-1}$
$\dot{\epsilon} = 1.0s^{-1}$
$\dot{\epsilon} = 0.6s^{-1}$
$5G_N^0$
$\Lambda_0 = 2.0$
$\Lambda_0 = 14.3$

Figure 9:

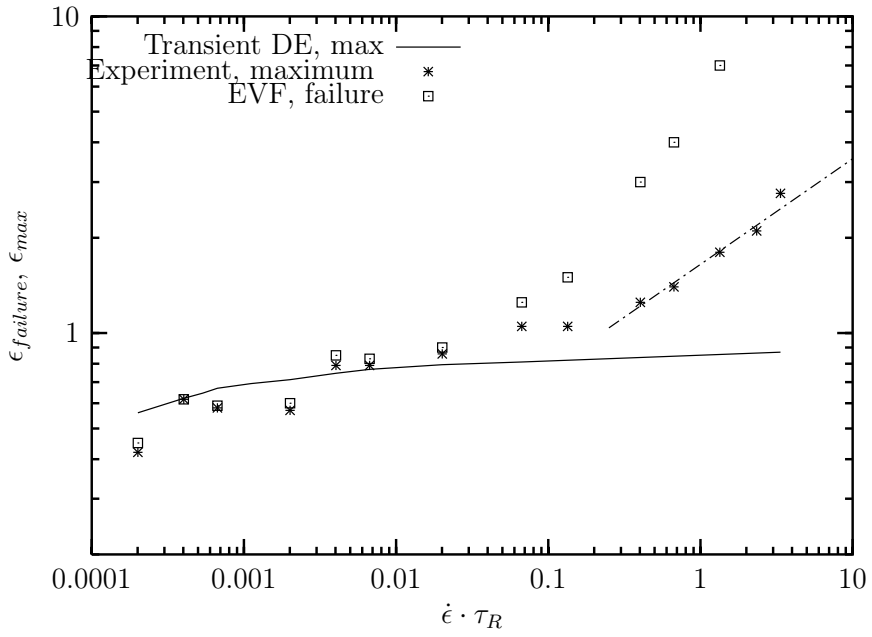
Transient DE, max
Experiment, maximum
EVF, failure
10
1
0.0001
0.001
0.01
0.1
1
10
$\epsilon_{failure}$, ϵ_{max}
$\dot{\epsilon} \cdot \tau_R$

Figure 10:

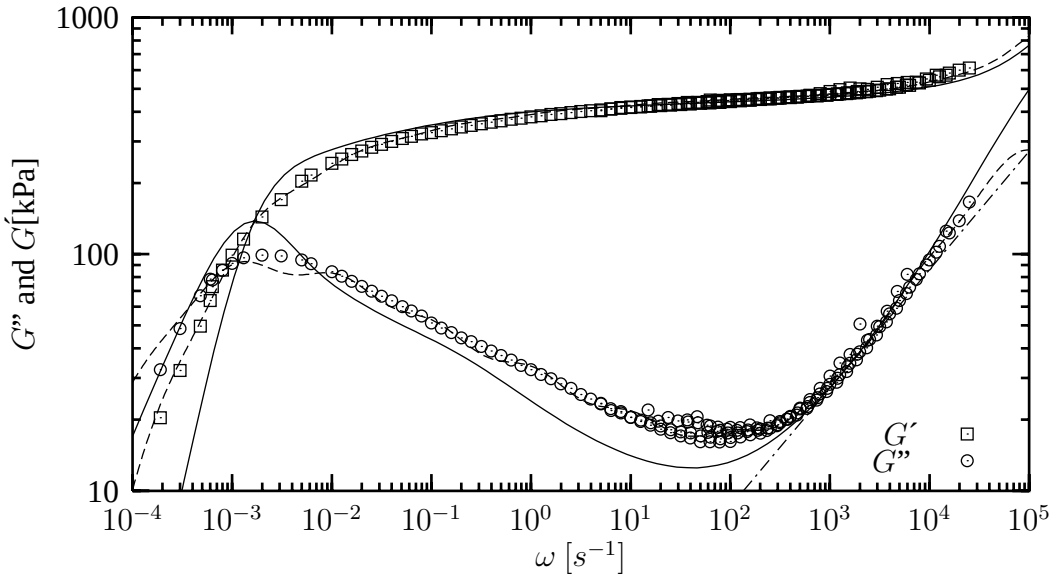
1000
100
10
G" and G´[kPa]
10^-4
10^-3
10^-2
10^-1
10^0
10^1
10^2
10^3
10^4
10^5
ω [s^-1]
G´
G"

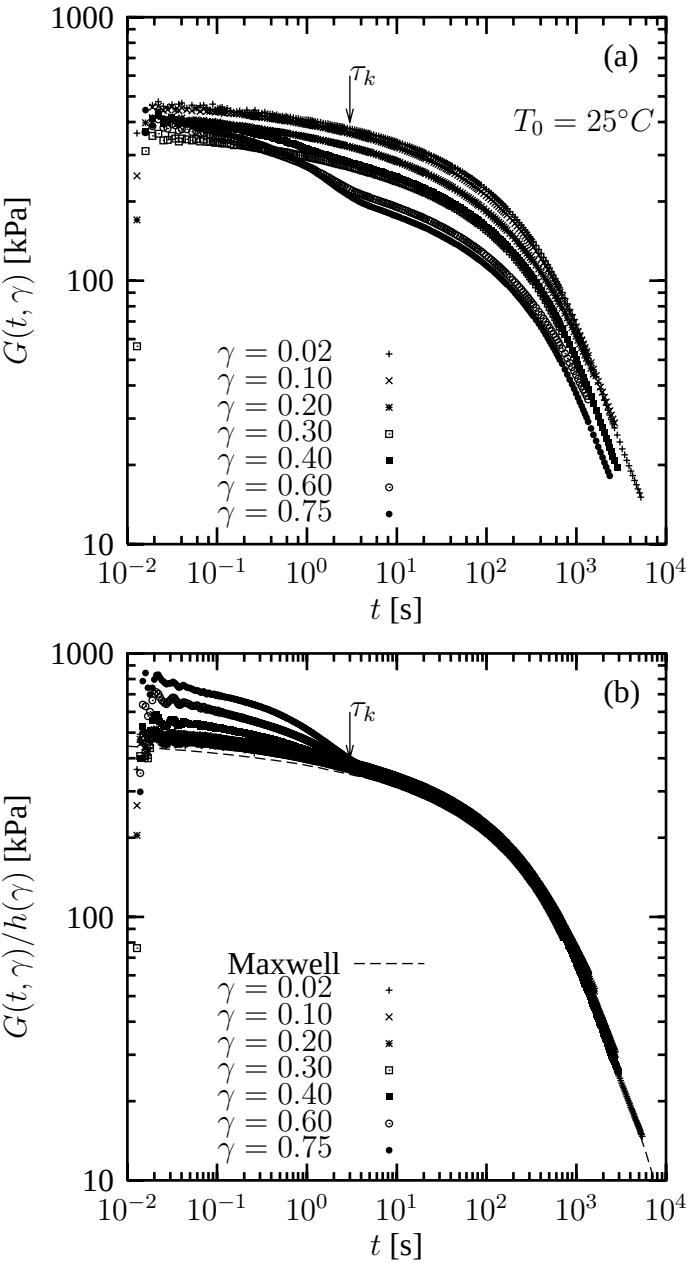
(a)
$T_0 = 25°C$
τ_k
$\gamma = 0.02$
$\gamma = 0.10$
$\gamma = 0.20$
$\gamma = 0.30$
$\gamma = 0.40$
$\gamma = 0.60$
$\gamma = 0.75$
$G(t,\gamma)$ [kPa]
t [s]
(b)
Maxwell
$G(t,\gamma)/h(\gamma)$ [kPa]

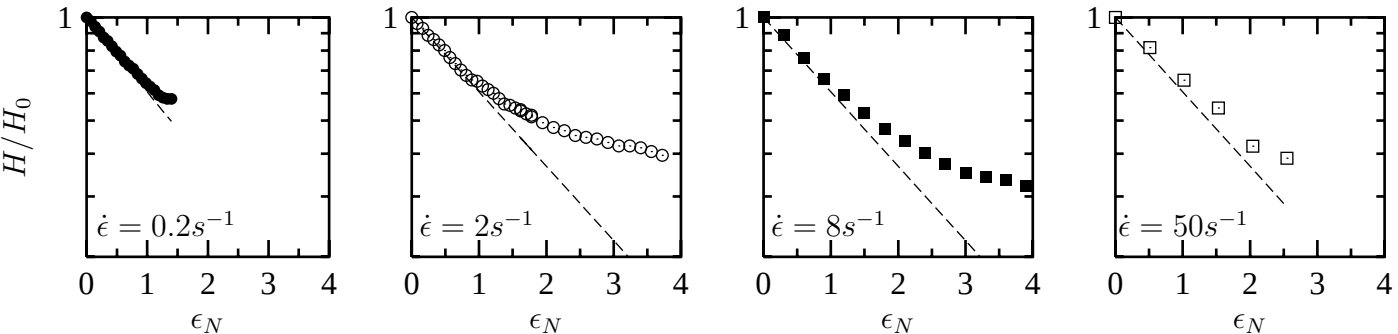
H/H_0
1
$\dot{\epsilon} = 0.2s^{-1}$
$\dot{\epsilon} = 2s^{-1}$
$\dot{\epsilon} = 8s^{-1}$
$\dot{\epsilon} = 50s^{-1}$
0
1
2
3
4
ϵ_N

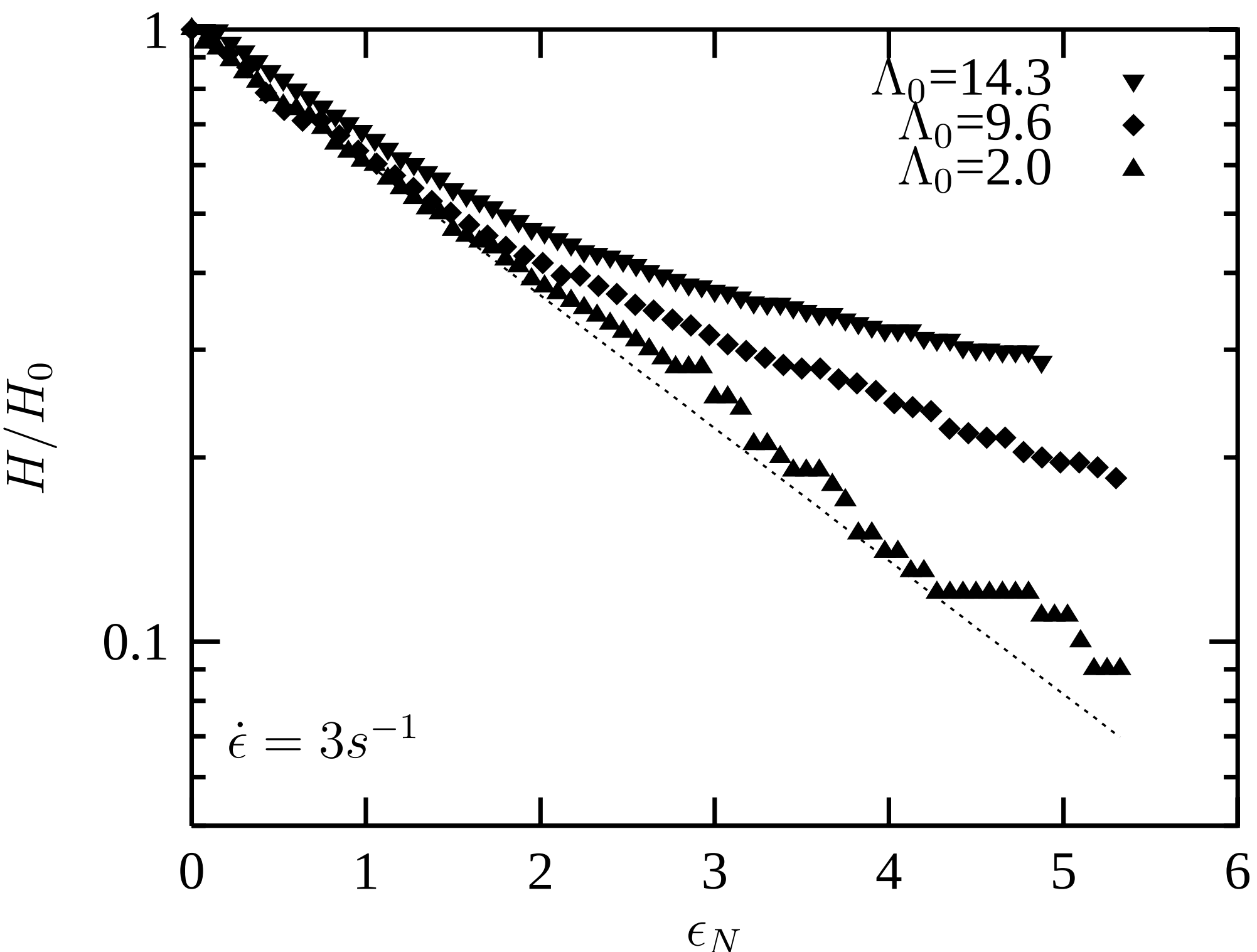
1
0.1
H/H_0
Λ_0=14.3
Λ_0=9.6
Λ_0=2.0
$\dot{\epsilon} = 3s^{-1}$
0
1
2
3
4
5
6
ϵ_N

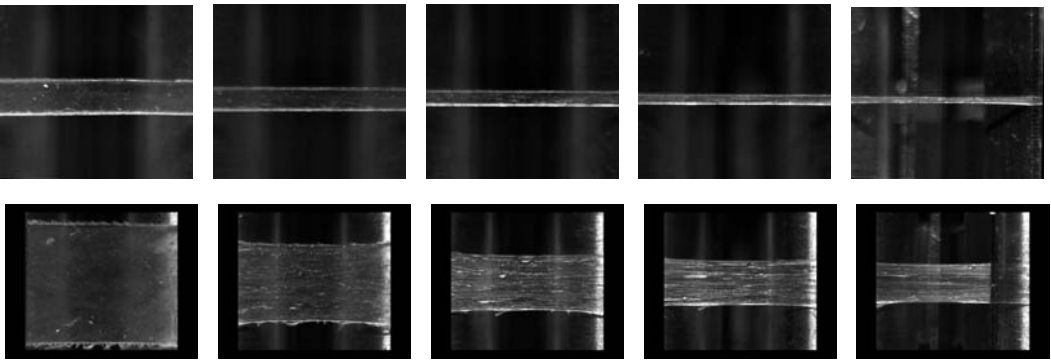

$\epsilon_N = 0$ $\epsilon_N = 1$ $\epsilon_N = 2$ $\epsilon_N = 3$ $\epsilon_N = 4$

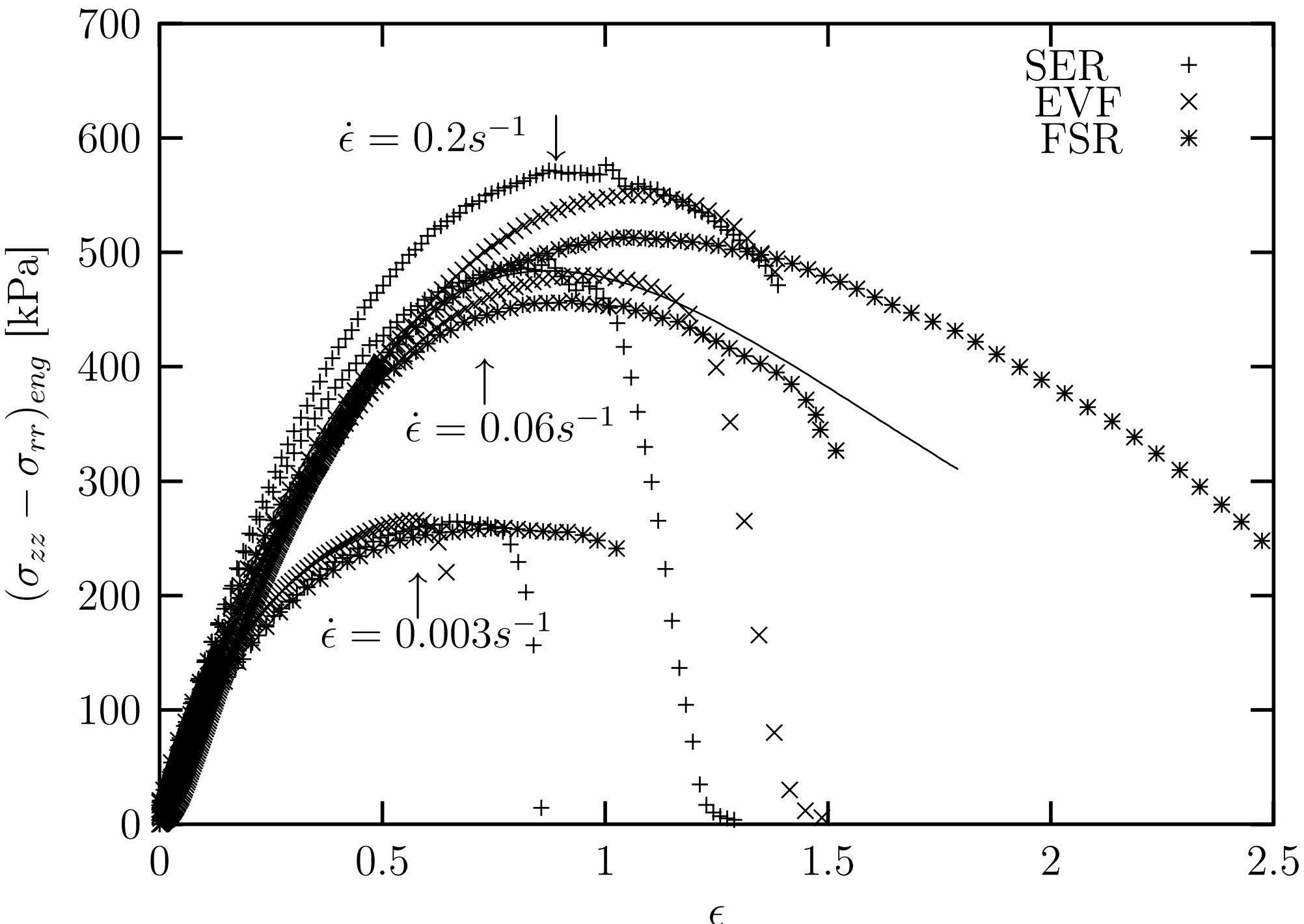
SER
EVF
FSR
$\dot{\epsilon} = 0.2s^{-1}$
$\dot{\epsilon} = 0.06s^{-1}$
$\dot{\epsilon} = 0.003s^{-1}$
$(\sigma_{zz} - \sigma_{rr})_{eng}$ [kPa]
ϵ
0
100
200
300
400
500
600
700
0
0.5
1
1.5
2
2.5

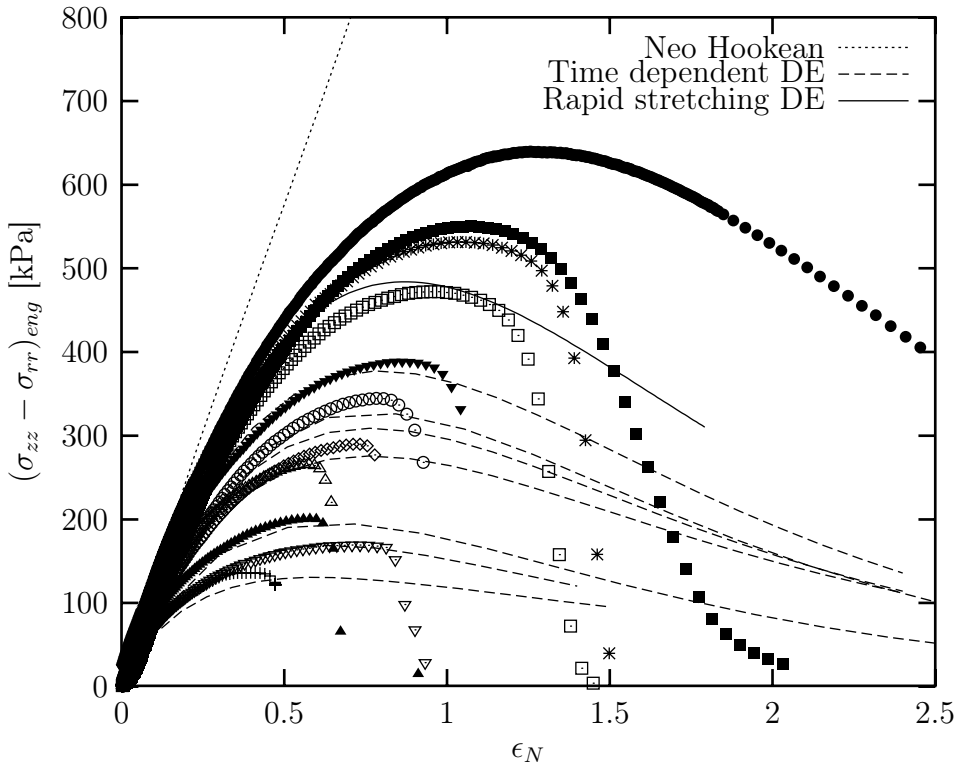

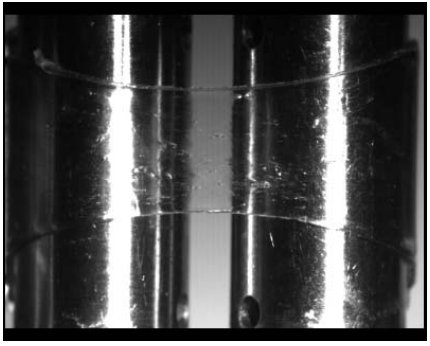

$\epsilon_N = 1.300$

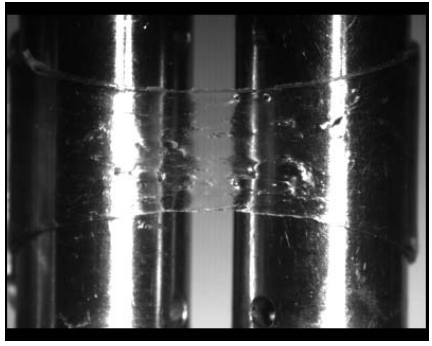

$\epsilon_N = 1.433$

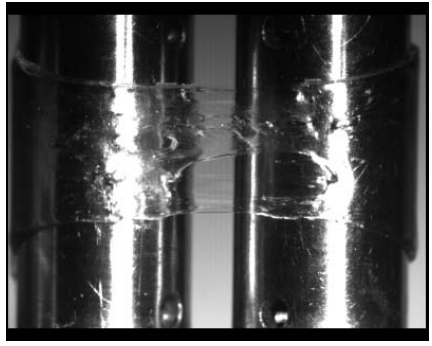

$\epsilon_N t = 1.567$

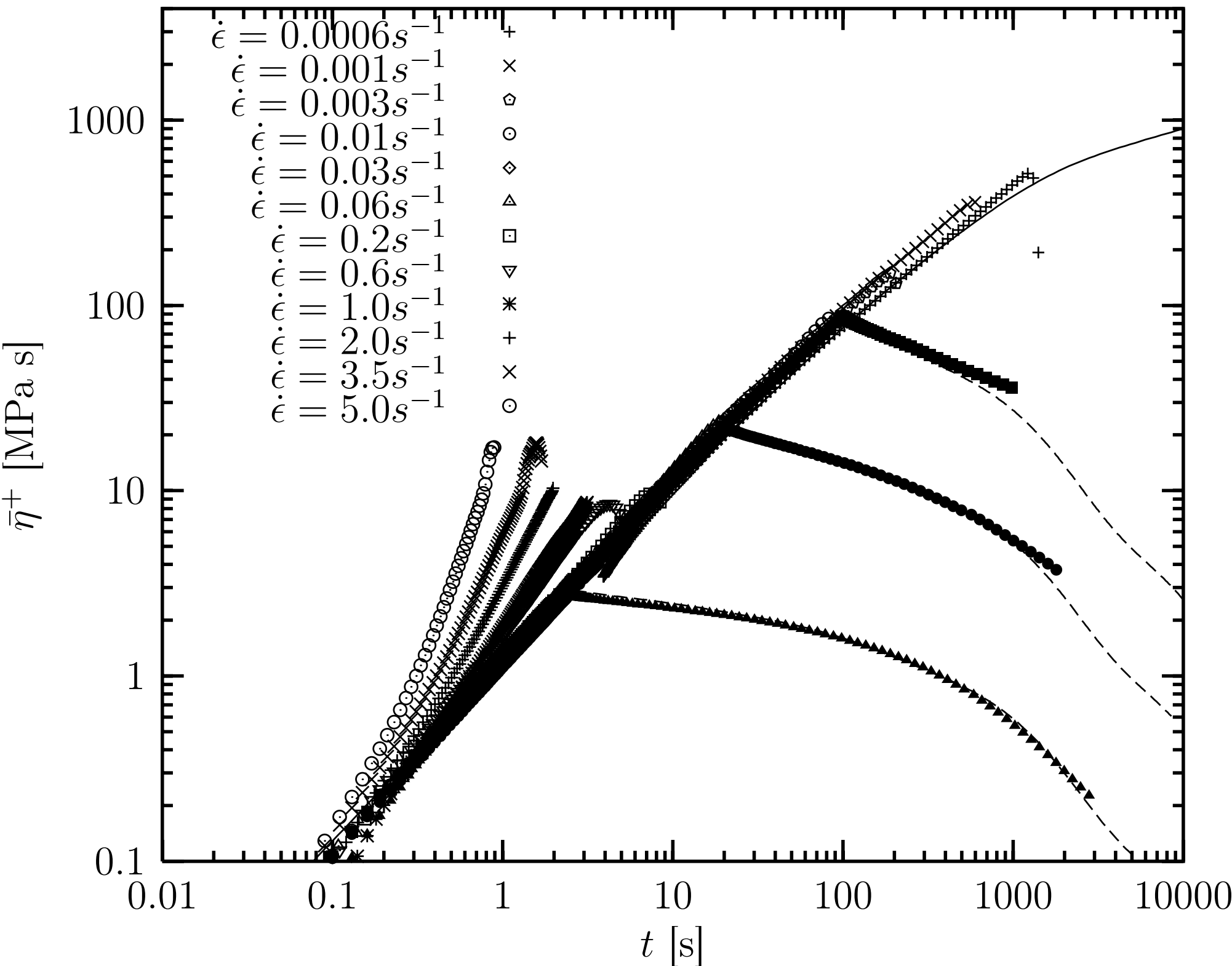
$\dot{\epsilon} = 0.0006s^{-1}$
$\dot{\epsilon} = 0.001s^{-1}$
$\dot{\epsilon} = 0.003s^{-1}$
$\dot{\epsilon} = 0.01s^{-1}$
$\dot{\epsilon} = 0.03s^{-1}$
$\dot{\epsilon} = 0.06s^{-1}$
$\dot{\epsilon} = 0.2s^{-1}$
$\dot{\epsilon} = 0.6s^{-1}$
$\dot{\epsilon} = 1.0s^{-1}$
$\dot{\epsilon} = 2.0s^{-1}$
$\dot{\epsilon} = 3.5s^{-1}$
$\dot{\epsilon} = 5.0s^{-1}$
1000
100
10
1
0.1
$\overline{\eta}^{+}$ [MPa s]
0.01
0.1
1
10
100
1000
10000
t [s]

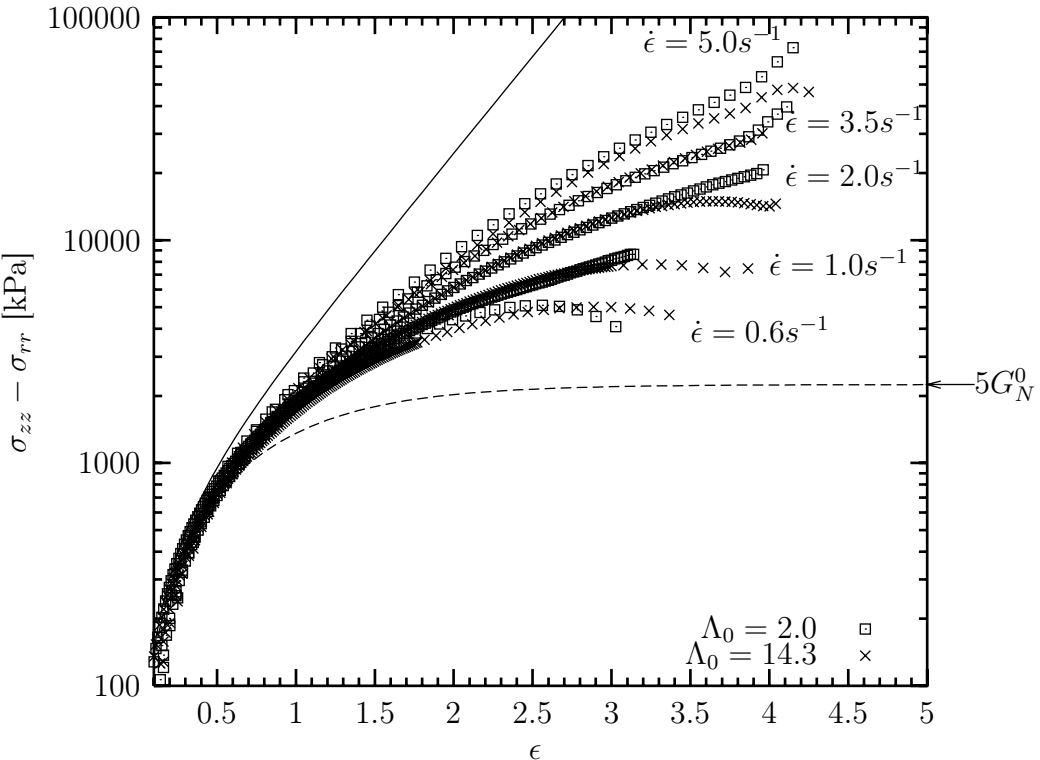
100000
10000
1000
100
$\sigma_{zz} - \sigma_{rr}$ [kPa]
0.5
1
1.5
2
2.5
3
3.5
4
4.5
5
ϵ
$\dot{\epsilon} = 5.0s^{-1}$
$\dot{\epsilon} = 3.5s^{-1}$
$\dot{\epsilon} = 2.0s^{-1}$
$\dot{\epsilon} = 1.0s^{-1}$
$\dot{\epsilon} = 0.6s^{-1}$
$5G_N^0$
$\Lambda_0 = 2.0$
$\Lambda_0 = 14.3$

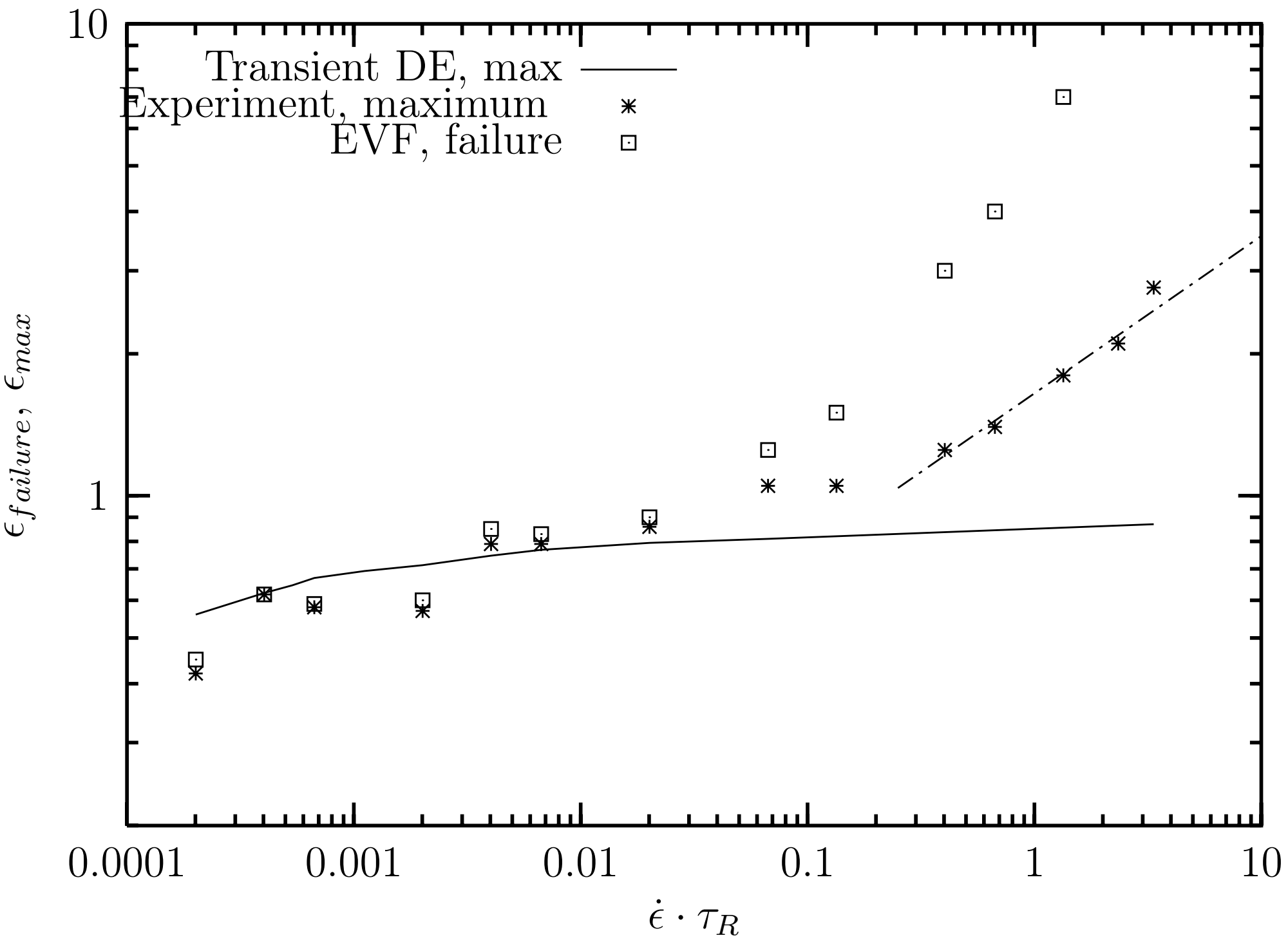
Transient DE, max
Experiment, maximum
EVF, failure
10
1
0.0001
0.001
0.01
0.1
1
10
$\epsilon_{failure}$, ϵ_{max}
$\dot{\epsilon} \cdot \tau_R$